**Figure 6.** Results of the simulation study demonstrating the effects of errors in the delay of the arterial input function (upper: **A–C**), errors of the assumed dispersion time constant (middle: **D–F**), and errors in the assumed partition coefficient ($p$ mL/g) (lower: **G–I**) on the calculated cerebral blood flow ($CBF$), oxygen extraction fraction ($OEF$), and metabolic rate of oxygen ($CMRO_2$) values. Positive and negative values of errors in delay time indicate overcorrection and undercorrection of delay time, respectively. Positive and negative values of errors in the time constant indicate undercorrection and overcorrection of dispersion time, respectively. Results are plotted for the dual-tracer autoradiographic (DARG) and the dual-tracer basis function methods (DBFM), for both the $H_2^{15}O$ ($C^{15}O_2$)–$^{15}O_2$ and $H_2^{15}O$–$^{15}O_2$ protocols.

acquired during sequential administration of dual tracers with $H_2^{15}O$ ($C^{15}O_2$)–$^{15}O_2$ and $^{15}O_2$–$H_2^{15}O$ protocols. Although further studies are needed, ability of eliminating additional $C^{15}O$ scan for $CBV$ assessment may contribute to improve the accuracy and applicability of the $CBF$, $OEF$, and $CMRO_2$ assessment in clinical settings.

## DISCLOSURE/CONFLICT OF INTEREST

The authors declare no conflict of interest.

## REFERENCES

1 Frackowiak RS, Jones T, Lenzi GL, Heather JD. Regional cerebral oxygen utilization and blood flow in normal man using oxygen-15 and positron emission tomography. *Acta Neurol Scand* 1980; **62**: 336–344.

2 Mintun MA, Raichle ME, Martin WR, Herscovitch P. Brain oxygen utilization measured with O-15 radiotracers and positron emission tomography. *J Nucl Med* 1984; **25**: 177–187.

3 Lammertsma AA, Heather JD, Jones T, Frackowiak RS, Lenzi GL. A statistical study of the steady state technique for measuring regional cerebral blood flow and oxygen utilisation using $^{15}O$. *J Comput Assist Tomogr* 1982; **6**: 566–573.

4 Subramanyam R, Alpert NM, Hoop B Jr., Brownell GL, Taveras JM. A model for regional cerebral oxygen distribution during continuous inhalation of $^{15}O_2$, $C^{15}O$, and $C^{15}O_2$. *J Nucl Med* 1978; **19**: 48–53.

5 Mintun MA, Lundstrom BN, Snyder AZ, Vlassenko AG, Shulman GL, Raichle ME. Blood flow and oxygen delivery to human brain during functional activity: theoretical modeling and experimental data. *Proc Nat Acad Sci USA* 2001; **98**: 6859–6864.

6 Hatazawa J, Fujita H, Kanno I, Satoh T, Iida H, Miura S *et al*. Regional cerebral blood flow, blood volume, oxygen extraction fraction, and oxygen utilization rate in

normal volunteers measured by the autoradiographic technique and the single breath inhalation method. *Ann Nucl Med* 1995; **9**: 15–21.

7 Hattori N, Bergsneider M, Wu HM, Glenn TC, Vespa PM, Hovda DA et al. Accuracy of a method using short inhalation of $^{(15)}$O-O$_{(2)}$ for measuring cerebral oxygen extraction fraction with PET in healthy humans. *J Nucl Med* 2004; **45**: 765–770.

8 Shimosegawa E, Hatazawa J, Ibaraki M, Toyoshima H, Suzuki A. Metabolic penumbra of acute brain infarction: a correlation with infarct growth. *Ann Neurol* 2005; **57**: 495–504.

9 Kudomi N, Hayashi T, Teramoto N, Watabe H, Kawachi N, Ohta Y et al. Rapid quantitative measurement of CMRO$_{(2)}$ and CBF by dual administration of $^{(15)}$O-labeled oxygen and water during a single PET scan-a validation study and error analysis in anesthetized monkeys. *J Cereb Blood Flow Metab* 2005; **25**: 1209–1224.

10 Iida H, Kanno I, Miura S. Rapid measurement of cerebral blood flow with positron emission tomography. *Ciba Foundation Symp* 1991; **163**: 23–37, discussion 37–42.

11 Koeppe RA, Holden JE, Ip WR. Performance comparison of parameter estimation techniques for the quantitation of local cerebral blood flow by dynamic positron computed tomography. *J Cereb Blood Flow Metab* 1985; **5**: 224–234.

12 Kudomi N, Choi E, Watabe H, Kim KM, Shidahara M, Ogawa M et al. Development of a GSO Detector Assembly for a Continuous Blood Sampling System. *IEEE TNS* 2003; **50**: 70–73.

13 Baron JC, Steinling M, Tanaka T, Cavalheiro E, Soussaline F, Collard P. Quantitative measurement of CBF, oxygen extraction fraction (OEF) and CMRO$_2$ with the O$^{15}$ continuous inhalation technique: experimental evidence and normal values in man. *J Cereb Blood Flow Metab* 1981; **1**: S5–S6.

14 West JB, Dollery CT. Uptake of oxygen-15-labeled CO$_2$ compared with carbon-11-labeled CO$_2$ in the lung. *J Appl Physiol* 1962; **17**: 9–13.

15 Shao L, Karp JS. Cross-plane scattering correction-point source deconvolution in PET. *IEEE Trans Med Imaging* 1991; **10**: 234–239.

16 Iida H, Kanno I, Miura S, Murakami M, Takahashi K, Uemura K. Error analysis of a quantitative cerebral blood flow measurement using H$_2^{(15)}$O autoradiography and positron emission tomography, with respect to the dispersion of the input function. *J Cereb Blood Flow Metab* 1986; **6**: 536–545.

17 Iida H, Higano S, Tomura N, Shishido F, Kanno I, Miura S et al. Evaluation of regional differences of tracer appearance time in cerebral tissues using [$^{15}$O] water and dynamic positron emission tomography. *J Cereb Blood Flow Metab* 1988; **8**: 285–288.

18 Kudomi N, Hayashi T, Watabe H, Teramoto N, Piao R, Ose T et al. A physiologic model for recirculation water correction in CMRO$_2$ assessment with $^{15}$O$_2$ inhalation PET. *J Cereb Blood Flow Metab* 2009; **29**: 355–364.

19 Kudomi N, Watabe H, Hayashi T, Iida H. Separation of input function for rapid measurement of quantitative CMRO$_2$ and CBF in a single PET scan with a dual tracer administration method. *Phys Med Biol* 2007; **52**: 1893–1908.

20 Phelps ME, Huang SC, Hoffman EJ, Kuhl DE. Validation of tomographic measurement of cerebral blood volume with C-11-labeled carboxyhemoglobin. *J Nucl Med* 1979; **20**: 328–334.

21 Kudomi N, Watabe H, Hayashi T, Oka H, Miyake Y, Iida H. Optimization of transmission scan duration for $^{15}$O PET study with sequential dual tracer administration using N-index. *Ann Nucl Med* 2010; **24**: 413–420.

22 Iida H, Law I, Pakkenberg B, Krarup-Hansen A, Eberl S, Holm S et al. Quantitation of regional cerebral blood flow corrected for partial volume effect using O-15 water and PET: I. Theory, error analysis, and stereologic comparison. *J Cereb Blood Flow Metab* 2000; **20**: 1237–1251.

23 Shidahara M, Watabe H, Kim KM, Oka H, Sago M, Hayashi T et al. Evaluation of a commercial PET tomograph-based system for the quantitative assessment of rCBF, rOEF and rCMRO$_2$ by using sequential administration of 15O-labeled compounds. *Ann Nucl Med* 2002; **16**: 317–327.

24 Ohta S, Meyer E, Thompson CJ, Gjedde A. Oxygen consumption of the living human brain measured after a single inhalation of positron emitting oxygen. *J Cereb Blood Flow Metab* 1992; **12**: 179–192.

25 Ohta S, Reutens DC, Gjedde A. Brief vibrotactile stimulation does not increase cortical oxygen consumption when measured by single inhalation of positron emitting oxygen. *J Cereb Blood Flow Metab* 1999; **19**: 260–265.

26 Meyer E, Tyler JL, Thompson CJ, Redies C, Diksic M, Hakim AM. Estimation of cerebral oxygen utilization rate by single-bolus $^{15}$O$_2$ inhalation and dynamic positron emission tomography. *J Cereb Blood Flow Metab* 1987; **7**: 403–414.

27 Fujita H, Kuwabara H, Reutens DC, Gjedde A. Oxygen consumption of cerebral cortex fails to increase during continued vibrotactile stimulation. *J Cereb Blood Flow Metab* 1999; **19**: 266–271.

28 Inomata T, Fijiwara M, Iida H, Kudomi N, Miura I. Neutron reduction of the small cyclotron for production of oxygen-15-1abeled gas. *Int Congress Series* 2004; **1265**: 97–100.

29 Miyake Y, Iida H, Hayashida K, Ishida Y. New method for the synthesis of $^{15}$O-1abeled carbon monoxide and $^{15}$O-1abeled dioxide for rapid supply in clinical use. *Int Congress Series* 2004; **1265**: 93–96.

30 Iguchi S, Hori Y, Moriguchi T, Morita N, Yamamoto A, Koshino K et al. Verification of a semi-automated MRI-guided technique for non-invasive determination of the arterial input function in $^{15}$O-labeled gaseous PET. *Nucl Instr Meth Phys Res* 2012 (in press).

31 Lammertsma AA, Wise RJ, Heather JD, Gibbs JM, Leenders KL, Frackowiak RS et al. Correction for the presence of intravascular oxygen-15 in the steady-state technique for measuring regional oxygen extraction ratio in the brain: 2. Results in normal subjects and brain tumour and stroke patients. *J Cereb Blood Flow Metab* 1983; **3**: 425–431.

32 Kudomi N, Slimani L, Jarvisalo MJ, Kiss J, Lautamaki R, Naum GA et al. Non-invasive estimation of hepatic blood perfusion from H$_2$ $^{15}$O PET images using tissue-derived arterial and portal input functions. *Eur J Nucl Med Mol Imaging* 2008; **35**: 1899–1911.

33 Kaisti KK, Langsjo JW, Aalto S, Oikonen V, Sipila H, Teras M et al. Effects of sevoflurane, propofol, and adjunct nitrous oxide on regional cerebral blood flow, oxygen consumption, and blood volume in humans. *Anesthesiology* 2003; **99**: 603–613.

34 Altman DI, Lich LL, Powers WJ. Brief inhalation method to measure cerebral oxygen extraction fraction with PET: accuracy determination under pathologic conditions. *J Nucl Med* 1991; **32**: 1738–1741.

35 Frykholm P, Andersson JL, Valtysson J, Silander HC, Hillered L, Persson L et al. A metabolic threshold of irreversible ischemia demonstrated by PET in a middle cerebral artery occlusion-reperfusion primate model. *Acta Neurol Scand* 2000; **102**: 18–26.

36 Pappata S, Fiorelli M, Rommel T, Hartmann A, Dettmers C, Yamaguchi T et al. PET study of changes in local brain hemodynamics and oxygen metabolism after unilateral middle cerebral artery occlusion in baboons. *J Cereb Blood Flow Metab* 1993; **13**: 416–424.

37 Schumann P, Touzani O, Young AR, Verard L, Morello R, MacKenzie ET. Effects of indomethacin on cerebral blood flow and oxygen metabolism: a positron emission tomographic investigation in the anaesthetized baboon. *Neurosci Lett* 1996; **220**: 137–141.

38 Touzani O, Young AR, Derlon JM, Beaudouin V, Marchal G, Rioux P et al. Sequential studies of severely hypometabolic tissue volumes after permanent middle cerebral artery occlusion. A positron emission tomographic investigation in anesthetized baboons. *Stroke* 1995; **26**: 2112–2119.

39 Young AR, Sette G, Touzani O, Rioux P, Derlon JM, MacKenzie ET et al. Relationships between high oxygen extraction fraction in the acute stage and final infarction in reversible middle cerebral artery occlusion: an investigation in anesthetized baboons with positron emission tomography. *J Cereb Blood Flow Metab* 1996; **16**: 1176–1188.

40 Cselenyi Z, Olsson H, Halldin C, Gulyas B, Farde L. A comparison of recent parametric neuroreceptor mapping approaches based on measurements with the high affinity PET radioligands [$^{11}$C]FLB 457 and [$^{11}$C]WAY 100635. *NeuroImage* 2006; **32**: 1690–1708.

41 Schuitemaker A, van Berckel BN, Kropholler MA, Kloet RW, Jonker C, Scheltens P et al. Evaluation of methods for generating parametric (R-[$^{11}$C]PK11195 binding images. *J Cereb Blood Flow Metab* 2007; **27**: 1603–1615.

# Preserved acetazolamide reactivity in lacunar patients with severe white-matter lesions: $^{15}$O-labeled gas and $H_2O$ positron emission tomography studies

Tomohisa Nezu[1,2], Chiaki Yokota[1], Toshiyuki Uehara[1], Miho Yamauchi[3], Kazuhito Fukushima[4], Kazunori Toyoda[1], Masayasu Matsumoto[2], Hidehiro Iida[3] and Kazuo Minematsu[1]

[1]Department of Cerebrovascular Medicine, National Cerebral and Cardiovascular Center, Suita, Japan; [2]Department of Clinical Neuroscience and Therapeutics, Hiroshima University Graduate School of Biomedical Sciences, Hiroshima, Japan; [3]Department of Bio-Medical Imaging, National Cerebral and Cardiovascular Center Research Institute, Suita, Japan; [4]Department of Radiology, National Cerebral and Cardiovascular Center, Suita, Japan

Limited evidence exists on the relationships between severity of white-matter lesions (WMLs) and cerebral hemodynamics in patients without major cerebral artery disease. To examine changes of cerebral blood flow (CBF), oxygen metabolism, and vascular reserve capacity associated with severity of WML in patients with lacunar stroke, we used a positron emission tomography (PET). Eighteen lacunar patients were divided into two groups according to the severity of WMLs, assessed by Fazekas classification; grades 0 to 1 as mild WML group and grades 2 to 3 as severe WML group. Rapid dual autoradiography was performed with $^{15}$O-labeled gas-PET followed by $^{15}$O-labeled water-PET with acetazolamide (ACZ) challenge. Compared with the mild WML group, the severe WML group showed lower CBF (20.6 ± 4.4 versus 29.9 ± 8.2 mL/100 g per minute, $P = 0.008$), higher oxygen extraction fraction (OEF) (55.2 ± 7.4 versus 46.7 ± 5.3%, $P = 0.013$), and lower cerebral metabolic rate of oxygen (CMRO$_2$) (1.95 ± 0.41 versus 2.44 ± 0.42 mL/100 g per minute, $P = 0.025$) in the centrum semiovale. There were no significant differences in the ACZ reactivity between the two groups (48.6 ± 22.6% versus 42.5 ± 17.2%, $P = 0.524$). Lacunar patients with severe WMLs exhibited reduced CBF and CMRO$_2$, and increased OEF in the centrum semiovale. The ACZ reactivity was preserved in both patients with severe and mild WMLs in each site of the brain.
*Journal of Cerebral Blood Flow & Metabolism* (2012) **32**, 844–850; doi:10.1038/jcbfm.2011.190; published online 18 January 2012

## Introduction

White-matter lesions (WMLs), observed as white-mater hyperintensity in T2-weighted magnetic reso-

Correspondence: Dr C Yokota, Department of Cerebrovascular Medicine, National Cerebral and Cardiovascular Center, 5-7-1 Fujishiro-dai, Suita, Osaka 565-8565, Japan.
E-mail: cyokota@hsp.ncvc.go.jp

nance imaging or fluid-attenuated inversion recovery (FLAIR) image, are commonly observed among elderly people (Hachinski *et al*, 1987). However, they are also associated with hypertension, diabetes, and other vascular risk factors (Murray *et al*, 2005; Pantoni and Garcia, 1997). Development of WMLs is known to be a cause of cognitive impairment, dementia, and disability (Prins *et al*, 2005). Recent studies showed that WMLs are not only a stroke risk factor (Streifler *et al*, 2002) but also a predictor of unfavorable stroke outcome (Koton *et al*, 2009). Despite accumulating evidence of the clinical significance of WMLs, the pathogenesis of WMLs has not been fully clarified.

Healthy elderly subjects with severe WMLs were reported to have reduced cerebral blood flow (CBF) and preservation of oxygen metabolism

(Meguro et al, 1990). Patients with dementia of the Binswanger type have marked decrease of both CBF and oxygen metabolism in the white matter; however, patients without dementia have a lesser decrease in CBF with preservation of almost-normal oxygen metabolism (Yao et al, 1992). These findings indicated that chronic hypoperfusion due to the progression of small artery disease is associated with the development of WMLs. In addition, hemo-dynamic disturbance induced by internal carotid artery occlusive disease was suggested to contribute to the development of extensive WMLs (Yamauchi et al, 1999).

Limited evidence exists on the relationships between severity of WMLs and hemodynamic disturbance in patients without major cerebral artery occlusive disease. Some studies showed that vascular reactivity was not related to severity of WMLs (Birns et al, 2009; Turc et al, 1994). Other studies reported that vascular reactivity in patients with severe WMLs is impaired (Bakker et al, 1999; Chabriat et al, 2000; Fu et al, 2006; Isaka et al, 1994; Kozera et al, 2010; Mochizuki et al, 1997). These inconsistencies may be due to differences in modalities for evaluation of vascular reserve capacity; i.e., transcranial Doppler ultrasound (Bakker et al, 1999; Birns et al, 2009; Fu et al, 2006; Kozera et al, 2010), perfusion MRI (Chabriat et al, 2000), xenon inhalation computed tomography (Isaka et al, 1994; Mochizuki et al, 1997), and single photon emission computed tomography (Turc et al, 1994). There are also differences in the vasodilatory stimulus used; i.e., $CO_2$ inhalation (Bakker et al, 1999), breath holding, hyperventilation tests (Birns et al, 2009; Kozera et al, 2010), and acetazolamide (ACZ) challenge test (Chabriat et al, 2000; Fu et al, 2006; Isaka et al, 1994; Mochizuki et al, 1997; Turc et al, 1994). Although single photon emission computed tomography study with ACZ challenge can detect stage II hemodynamic failure (Powers, 1991) by positron emission tomography (PET) in patients with major cerebral artery occlusive disease (Hirano et al, 1994), the relationship between ACZ reactivity and oxygen metabolism in patients with WMLs without major artery disease has not been elucidated. We hypothesized that either impairment of vascular reserve capacity or chronic hypoperfusion in the white matter contributes to the development of WMLs without major artery disease.

The aim of this study was to examine the changes of CBF, oxygen metabolism, and vascular reserve capacity associated with the severity of WMLs in patients with lacunar stroke.

## Materials and methods

### Patients

This study was a single-center hospital-based prospective study. The study protocol was governed by the guidelines of national government based on the Helsinki Declaration revised in 1983, and it was approved by the Institutional Research and Ethics Committee of our hospital. All patients gave written informed consent to participate in the study. Patients with lacunar stroke, at least 3 weeks after the onset, were enrolled between April 2009 and April 2010. All patients underwent PET studies with $^{15}$O-labeled gas ($C^{15}O_2$, $^{15}O_2$, $C^{15}O$) inhalation and $^{15}$O-water with ACZ challenge autoradiography as described previously (Kudomi et al, 2005, 2007), as well as MRI studies. Lacunar stroke was defined as a typical clinical syndrome associated with a small infarct, < 15 mm in diameter on MRI, restricted to the territory of a perforating artery without adjacent major artery occlusive lesions. Patients with stenosis (> 50% in diameter) or occlusion of the internal carotid artery or the trunk of the middle cerebral artery on magnetic resonance angiography or ultrasonography were excluded from the study. The median time interval between the onset of stroke and PET studies was 1,017 days (interquatile range 519 to 1,856).

Baseline clinical characteristics including age, sex, hypertension, diabetes mellitus, dyslipidemia, and current smoking were recorded. Information of risk factors and medical history was collected from a self-reported medical history or inferred from prescribed medication by the primary physicians. Criteria for hypertension, diabetes mellitus, and dyslipidemia were as previously defined (Yokota et al, 2009). Cognitive function was evaluated in all patients by the mini-mental state examination (Folstein et al, 1975) and clinical dementia rating (Hughes et al, 1982). Dementia was defined as clinical dementia rating ≥ 1, and patients with dementia met the criteria proposed by National Institute of Neurological and Communicative Disorders and Stroke and the Alzheimer's Disease and Related Disorders Association (NINCDS-ADRDA Alzheimer's Criteria) (Roman et al, 1993).

### Magnetic Resonance Imaging

Magnetic resonance imaging was performed on a 1.5-T scanner (Magnetom Vision or Magnetom Sonata; Siemens Medical Systems, Erlangen, Germany). The imaging protocol consisted of a T1-weighted spin-echo, a T2-weighted spin-echo, and FLAIR image. Severity of WMLs was assessed using the FLAIR (repetition time 900 ms, echo time 119 ms, field-of-view 230 × 201 mm$^2$, matrix 256 × 210, 4 mm slice thickness, and 2 mm gap between slices).

Two investigators (CY and TN), who were unaware of all clinical data, graded the degree of severity of WMLs by visual inspection using the Fazekas classification of WMLs as follows: none (grade 0), punctate (grade 1), early confluent (grade 2), and confluent lesions (grade 3) (Fazekas et al, 1987). The patients with grades 0 to 1 were defined as the mild WMLs group and those with grades 2 to 3 were defined as the severe WMLs group. Additionally, WMLs volume was measured manually based on FLAIR imaging (20 slices) using Dr View/LINUX software (AJS, Ver R2.5, Tokyo, Japan).

846

## Positron Emission Tomography Imaging

We used an ECAT47 PET scanner (Siemens Medical Systems), which provided an intrinsic spatial resolution of 4.5 mm full-width at half-maximum at the center of the field-of-view. Data were acquired in 2D mode, and corrected for scatter compensation. A catheter was placed in the brachial artery for continuous monitoring of the arterial blood radioactivity concentration and arterial input function using a scintillator block detector system (BeCON; Molecular Imaging Labo, Suita, Japan) (Kudomi et al, 2003).

Quantitative images of CBF and oxygen extraction fraction (OEF) were obtained from a series of PET scans with $^{15}O$-labeled gas ($C^{15}O_2$, $^{15}O_2$, and $C^{15}O$) inhalation after a rapid dual autoradiography protocol as reported in a series of publications by Kudomi et al (2005, 2007). Briefly, after a 10-minute transmission scan for the attenuation correction and an $^{15}O$-labeled carbon monoxide ($C^{15}O$) scan for the blood volume assessment, a single dynamic scan was performed for 8 minutes, during which 4,000 MBq of oxygen ($^{15}O_2$) and 5,000 MBq of $^{15}O$-labeled carbon dioxide ($C^{15}O_2$) gases were inhaled each > 1 minute, sequentially at an interval of 5 minutes. Time to complete the whole dual autoradiography protocol was ~40 minutes. Cerebral metabolic rate of oxygen ($CMRO_2$) was calculated by multiplying the arterial oxygen content to the product images of OEF times CBF.

Additionally, two sets of PET scans were performed, each followed with $^{15}O$-labeled water injection to assess regional CBF images using $^{15}O$-water autoradiography (Kanno et al, 1987). The first scan was initiated without any pharmacological or physiological stress (at rest) and the second scan was performed at 10 minutes after an intravenous injection of ACZ titrated to 17 mg/kg. Physiological and laboratory data such as blood pressure, heart rate, and blood gas analysis (Siemens RAPIDLab 1265; Siemens Medical Systems) were obtained during the PET study.

## Data Analysis

The small circular regions of interest (ROIs) (10 mm in diameter) were placed in the frontal cortex, parietal cortex, occipital cortex, basal ganglia, and centrum semiovale based on automatic registration of MRI to PET by using PVElab (the PVEOut Consortium) (Quarantelli et al, 2004; Svarer et al, 2005). The program is followed by automatic segmentation (running with Statistical Parametric Mapping 5 (SPM5) Software (Institute of Neurology, University College of London, London, UK) and correction of PET counts for fractional volume as determined from the segmentation. The ROIs were manually placed on the FLAIR images and transferred to the CBF images for analysis (Figure 1). We defined the ACZ reactivity as the percentage increase in CBF after ACZ administration relative to baseline CBF. In each subject, the mean measures were obtained by averaging the values for both hemispheres.

## Statistical Analysis

Statistical analysis was performed using JMP 7.0 software (SAS Institute, Cary, NC, USA). The statistical significance of intergroup differences was assessed by $\chi^2$ tests, unpaired $t$-tests, and the Mann–Whitney $U$-test, as appropriate. Logarithmic transformation was performed on WMLs volumes, which was a skewed variable. The relationship between each parameter of PET and log-WML was examined by Pearson's correlation. A value of $P < 0.05$ was considered statistically significant.

# Results

Patients were divided into two groups of severe WMLs ($n = 9$) and mild WMLs ($n = 9$) on the basis of MRI findings. There were no significant differences in age, sex, and vascular risk factors between the two groups (Table 1). Three patients with dementia defined as clinical dementia rating $\geq 1$ were enrolled in the severe WMLs group; however, the rating of mini-mental state examination was not significantly different between the two groups. There were no significant differences in baseline CBF values between the gas-PET and $H_2O$-PET results. Compared with patients in the mild WMLs group, the patients
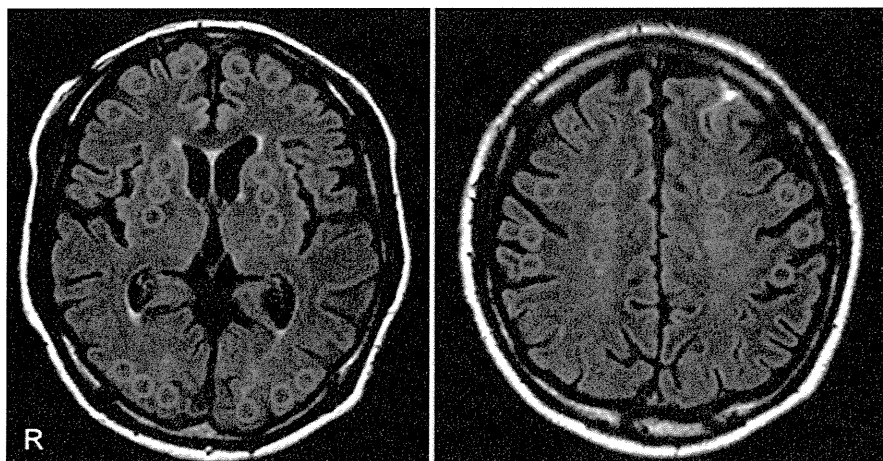


Figure 1 Regions of interest (ROIs) on fluid-attenuated inversion recovery (FLAIR). The small circular ROIs (10 mm in diameter) were placed on the frontal cortex, parietal cortex, occipital cortex, basal ganglia, and the centrum semiovale based on FLAIR image.

**Table 1** Baseline characteristics

|  | Severe WMLs group (n = 9) | Mild WMLs group (n = 9) | P |
|---|---|---|---|
| Age (years) | 76 (73–78) | 74 (70–77) | 0.329 |
| Male | 6 (67) | 8 (89) | 0.577 |
| Current smoker | 7 (78) | 7 (78) | 0.999 |
| Hypertension | 9 (100) | 8 (88) | 0.999 |
| Diabetes mellitus | 3 (33) | 3 (33) | 0.999 |
| Dyslipidemia | 6 (67) | 6 (67) | 0.999 |
| WMLs (cm³) | 33.3 (21.5–90.9) | 3.1 (1.3–4.4) | 0.003 |
| History of stroke | 3 (33) | 2 (22) | 0.999 |
| Time interval between stroke onset and PET study (days) | 953 (445–1,958) | 1,017 (519–1,623) | 0.847 |
| MMSE | 24.0 (20.5–28.5) | 28.0 (24.5–29.5) | 0.140 |
| CDR | 0.5 (0–1) | 0 (0–0.5) | 0.185 |
| Dementia | 3 (33) | 0 (0) | 0.206 |

WMLs, white-matter lesions; PET, positron emission tomography; MMSE, mini-mental state examination; CDR, clinical dementia rating.
Data are number of patients (%), median (interquartile range) for discontinuous variables.

in the severe WMLs group had lower CBF ($20.6 \pm 4.4$ versus $29.9 \pm 8.2$ mL/100 g per minute, $P = 0.008$), higher OEF ($55.2 \pm 7.4$ versus $46.7 \pm 5.3\%$, $P = 0.013$), and lower $CMRO_2$ ($1.95 \pm 0.41$ versus $2.44 \pm 0.42$ mL/100 g per minute, $P = 0.025$) in the centrum semiovale, by gas-PET study (Table 2). There were no significant differences in any other parameters of the gas-PET in other ROIs between the two groups. Cerebral blood flow and $CMRO_2$ had a negative correlation with the severity of WMLs, and OEF had a positive correlation with the severity of WMLs (Figure 2). There were no significant differences in ACZ reactivity between the severe and mild WMLs groups in each site of the brain by $H_2O$-PET examination (Table 3). The results of physiological data and blood gas analysis during ACZ challenge were comparable between the two groups (data not shown). The ACZ reactivity was not correlated with the OEF or with the severity of WMLs ($P = 0.422$ and $P = 0.316$, respectively) (Figure 3).

## Discussion

This study showed reduced CBF, reduced $CMRO_2$, and increased OEF in patients with severe WMLs compared with those with mild WMLs in the centrum semiovale. All patients in this study had lacunar stroke without major cerebral artery disease. The study also showed that ACZ reactivity was not impaired in either the cortex or the white matter of the patients of both groups.

Hatazawa *et al* (1997) found asymptomatic WMLs subjects exhibited reduction of CBF in the white matter and basal ganglia without decrease in $CMRO_2$. They also observed an increase in OEF in these areas, suggesting a chronic hypoperfusion in these territories. The present study provided additional information of reduction of both CBF and $CMRO_2$ with an increase in OEF in the WML in the patient groups with severe WMLs. Centrum semiovale is

**Table 2** Comparison of each parameter of the gas-PET study between patients with severe or mild WMLs in the brain

|  | Severe WMLs group (n = 9) | Mild WMLs group (n = 9) | P |
|---|---|---|---|
| *Frontal cortex* |  |  |  |
| CBF (mL/100 g per minute) | $35.7 \pm 9.0$ | $37.8 \pm 8.5$ | 0.630 |
| CBV (mL/100 g) | $3.0 \pm 0.9$ | $3.0 \pm 0.6$ | 0.969 |
| OEF (%) | $54.1 \pm 14.7$ | $48.3 \pm 5.2$ | 0.275 |
| $CMRO_2$ (mL/100 g per minute) | $3.24 \pm 0.49$ | $3.26 \pm 0.73$ | 0.946 |
| *Parietal cortex* |  |  |  |
| CBF | $40.2 \pm 6.9$ | $44.1 \pm 11.6$ | 0.403 |
| CBV | $2.8 \pm 0.7$ | $3.1 \pm 0.5$ | 0.284 |
| OEF | $50.6 \pm 6.9$ | $46.3 \pm 4.9$ | 0.146 |
| $CMRO_2$ | $3.53 \pm 0.35$ | $3.62 \pm 0.80$ | 0.743 |
| *Occipital cortex* |  |  |  |
| CBF | $40.4 \pm 8.6$ | $47.4 \pm 16.1$ | 0.266 |
| CBV | $3.5 \pm 0.9$ | $3.7 \pm 1.5$ | 0.745 |
| OEF | $55.8 \pm 8.8$ | $50.4 \pm 4.5$ | 0.116 |
| $CMRO_2$ | $3.88 \pm 0.63$ | $4.22 \pm 1.16$ | 0.442 |
| *Basal ganglia* |  |  |  |
| CBF | $45.1 \pm 9.4$ | $49.5 \pm 13.1$ | 0.426 |
| CBV | $2.3 \pm 0.7$ | $2.5 \pm 0.5$ | 0.521 |
| OEF | $52.8 \pm 7.9$ | $50.5 \pm 6.3$ | 0.505 |
| $CMRO_2$ | $4.14 \pm 0.66$ | $4.43 \pm 0.90$ | 0.441 |
| *Centrum semiovale* |  |  |  |
| CBF | $20.6 \pm 4.4$ | $29.9 \pm 8.2$ | 0.008 |
| CBV | $1.2 \pm 0.4$ | $1.4 \pm 0.3$ | 0.217 |
| OEF | $55.2 \pm 7.4$ | $46.7 \pm 5.3$ | 0.013 |
| $CMRO_2$ | $1.95 \pm 0.41$ | $2.44 \pm 0.42$ | 0.025 |

CBF, cerebral blood flow; CBV, cerebral blood volume; $CMRO_2$, cerebral metabolic rate of oxygen; OEF, oxygen extraction fraction; PET, positron emission tomography; WMLs, white-matter lesions.
*P* value by Mann–Whitney *U*-test.

located at the border of an area supplied by deep perforating arteries and the terminal branches of the middle cerebral artery. A decrease in CBF with reduction of $CMRO_2$ in the centrum semiovale in the present study should indicate a consequence of a reduced tissue metabolism in this terminal zone.

In the present study, patients with severe WMLs without major artery disease had increased OEF showed by gas-PET; however, their ACZ reactivity by $H_2O$-PET was preserved. The vascular reserve capacity evaluated by ACZ reactivity was preserved in both patients with severe and mild WMLs. Reduction of both CBF and $CMRO_2$ in the white matter was previously shown in patients with the Binswanger type dementia (Yao *et al*, 1990), being consistent with our results. Postmortem neuropathologic studies have shown decreased neuronal connectivity in the white matter in progressive subcortical vascular encephalopathy of Binswanger type (Yamanouchi *et al*, 1989, 1990). Functional reduction in cortical neuronal activity due to disruption of connections between the cortex and subcortex, as indicated previously (Pozzilli *et al*, 1987; Sette *et al*, 1989), is likely to be associated with a reduction of $CMRO_2$ in the centrum semiovale
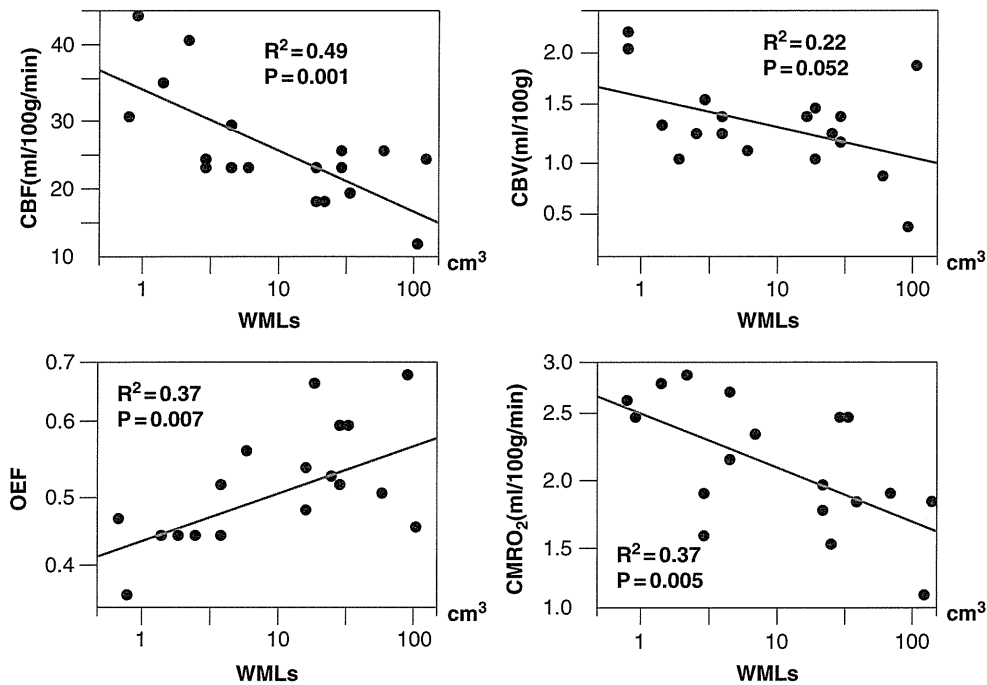
**Figure 2** Correlation between WML volume and each gas-PET parameter in the centrum semiovale. CBF and $CMRO_2$ had a negative correlation with the severity of WMLs, while OEF was positively correlated with the severity of WMLs. CBF, cerebral blood flow; CBV, cerebral blood volume; OEF, oxygen extraction fraction; $CMRO_2$, cerebral metabolic rate of oxygen; WMLs, white-matter lesions; PET, positron emission tomography.

**Table 3** Comparison of CBF between patients with severe or mild WMLs in the brain by $H_2O$-PET

| | Severe WMLs group (n = 9) | Mild WMLs group (n = 9) | P |
|---|---|---|---|
| Frontal cortex | | | |
| CBF baseline | 36.1 ± 7.2 | 40.2 ± 7.3 | 0.244 |
| CBF ACZ | 58.5 ± 10.2 | 59.9 ± 10.3 | 0.770 |
| ACZ reactivity (%) | 64.6 ± 28.5 | 49.7 ± 14.9 | 0.183 |
| Parietal cortex | | | |
| CBF baseline | 39.7 ± 4.8 | 45.7 ± 10.5 | 0.136 |
| CBF ACZ | 62.0 ± 7.1 | 66.9 ± 14.6 | 0.387 |
| ACZ reactivity (%) | 57.2 ± 17.1 | 47.1 ± 13.5 | 0.181 |
| Occipital cortex | | | |
| CBF baseline | 38.1 ± 7.1 | 45.7 ± 11.5 | 0.109 |
| CBF ACZ | 61.7 ± 13.3 | 70.1 ± 17.0 | 0.259 |
| ACZ reactivity (%) | 62.2 ± 21.5 | 54.2 ± 16.6 | 0.392 |
| Basal ganglia | | | |
| CBF baseline | 47.1 ± 9.8 | 54.6 ± 11.3 | 0.148 |
| CBF ACZ | 73.7 ± 10.5 | 85.7 ± 24.6 | 0.200 |
| ACZ reactivity (%) | 60.9 ± 31.0 | 55.7 ± 22.9 | 0.694 |
| Centrum semiovale | | | |
| CBF baseline | 19.0 ± 4.1 | 29.8 ± 9.2 | 0.005 |
| CBF ACZ | 28.5 ± 5.9 | 41.8 ± 10.9 | 0.005 |
| ACZ reactivity (%) | 48.6 ± 22.6 | 42.5 ± 17.2 | 0.524 |

ACZ, acetazolamide; CBF, cerebral blood flow; PET, positron emission tomography; WMLs, white-matter lesions.
P value by Mann–Whitney U-test.

in the patients with severe WMLs. Furthermore, the cerebral vessels would not dilate during fluctuations in systemic arterial pressure in daily life in these conditions of disruption of connections. Chronic hypoperfusion with a reduction of $CMRO_2$ in accordance with a disconnection between the cortex and subcortex may be the cause of development of WMLs without major artery disease.

To our knowledge, this is the first report of alterations in CBF, $CMRO_2$, and OEF, with preservation of ACZ reactivity in patients with mild or severe WMLs, with careful consideration of possible methodological errors. Indeed, quantitation of physiological parameters using PET is still a challenging issue, particularly in the white-matter area. As shown in earlier studies (Herscovitch and Raichle, 1983; Huang et al, 1987), the absolute values of both CBF and $CMRO_2$ could be biased because the spatial resolution of PET devices is limited compared with the physical size of the brain tissue component, or the partial volume effects. Oxygen extraction fraction is relatively stable and is less affected by partial volume effects. Our observation of increased OEF could not be explained by partial volume effects alone. Scatter is smaller in 2D mode in PET as compared with 3D acquisition. In this study, scatter correction was applied to minimize the contribution of radioactivity from the surrounding tissue components due to scatter. The ROIs were placed carefully with a guide of anatomical MRI to
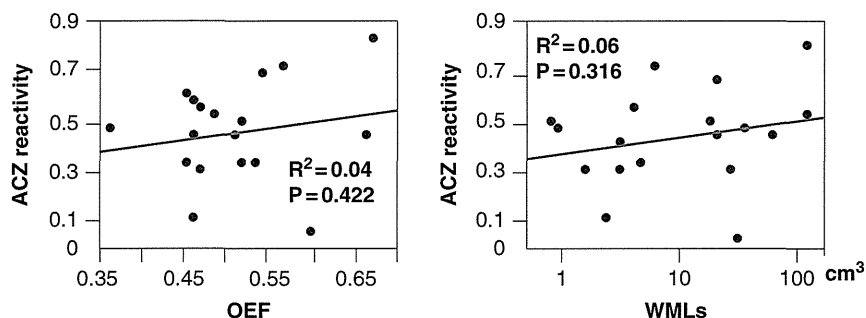
**Figure 3** The correlation between ACZ reactivity and OEF or WML volume in the centrum semiovale. Neither OEF nor WML volume was correlated with ACZ reactivity. ACZ, acetazolamide; OEF, oxygen extraction fraction; WMLs, white-matter lesions.

minimize the errors arising from radioactivity counts of surrounding tissues. These factors remain concerns to be dealt with in future investigations.

There are several issues that need to be addressed, as follows. First, we intended to avoid possible bias in the patient selection, but a relatively small number of subjects could cause selection bias despite our efforts. Second, three patients with dementia were enrolled in the severe WMLs group. Because oxygen metabolism in demented patients was reported to be different from that in non-demented patients (Yao et al, 1992), a reduced $CMRO_2$ with reduced CBF in the severe WMLs group could be attributed to secondary effects arising from decreased cognitive function. Third, we examined the vascular reserve capacity by ACZ challenge. Recently, ACZ-induced vasodilation was reported not to inhibit the visually evoked flow response (Yonai et al, 2010), which indicates that the vasodilatory mechanism during neurovascular coupling may be different from the mechanism of ACZ-induced vasodilation. Acetazolamide at a dose of 17 mg/kg would not cause maximal cerebral vasodilatation. However, there were no significant differences in ACZ reactivity between the two groups, and ACZ reactivity was preserved in all patients in the present study. Fourth, PET imaging in the present study was a single scatter subtraction technique based on the Klein–Nishina formulation which was implemented in the reconstruction software (Watson, 2000). This technique was shown to provide reasonable accuracy in several phantom experiments. It should also be noted that the data were acquired in 2D mode, which has much smaller amount of scatter as compared with recently available 3D mode. Further, the filtered-back projection technique was applied for the image reconstruction. In this procedure, the scatter contribution is likely reduced in the reconstructed images. However, limited spatial resolution of PET devices is a significant source of errors that causes possible contamination of radioactivity counts of cortical grey matter tissue. Exact magnitude of errors in the calculated parameters in the WML cannot be well defined. In addition, PET scanning in the present study has not been applied to age-matched normal subjects. Further systematic study is needed.

In conclusion, we showed that there is reduced CBF and $CMRO_2$, and increased OEF in the centrum semiovale of patients with severe WMLs compared with patients with mild WMLs. The ACZ reactivity was preserved in both patients with severe and mild WMLs. Further studies will be needed to clarify the pathogenesis of WMLs.

## Disclosure/conflict of interest

The authors declare no conflict of interest.

## References

Bakker SL, de Leeuw FE, de Groot JC, Hofman A, Koudstaal PJ, Breteler MM (1999) Cerebral vasomotor reactivity and cerebral white matter lesions in the elderly. Neurology 52:578–83

Birns J, Jarosz J, Markus HS, Kalra L (2009) Cerebrovascular reactivity and dynamic autoregulation in ischaemic subcortical white matter disease. J Neurol Neurosurg Psychiatry 80:1093–8

Chabriat H, Pappata S, Ostergaard L, Clark CA, Pachot-Clouard M, Vahedi K, Jobert A, Le Bihan D, Bousser MG (2000) Cerebral hemodynamics in CADASIL before and after acetazolamide challenge assessed with MRI bolus tracking. Stroke 31:1904–12

Fazekas F, Chawluk JB, Alavi A, Hurtig HI, Zimmerman RA (1987) MR signal abnormalities at 1.5 T in Alzheimer's dementia and normal aging. AJR Am J Roentgenol 149:351–6

Folstein MF, Folstein SE, McHugh PR (1975) 'Mini-mental state'. A practical method for grading the cognitive state of patients for the clinician. J Psychiatr Res 12:189–98

Fu JH, Lu CZ, Hong Z, Dong Q, Ding D, Wong KS (2006) Relationship between cerebral vasomotor reactivity and white matter lesions in elderly subjects without large artery occlusive disease. J Neuroimaging 16:120–5

Hachinski VC, Potter P, Merskey H (1987) Leuko-araiosis. Arch Neurol 44:21–3

Hatazawa J, Shimosegawa E, Satoh T, Toyoshima H, Okudera T (1997) Subcortical hypoperfusion associated with asymptomatic white matter lesions on magnetic resonance imaging. Stroke 28:1944–7

Herscovitch P, Raichle ME (1983) Effect of tissue heterogeneity on the measurement of cerebral blood flow with the equilibrium C15O2 inhalation technique. J Cereb Blood Flow Metab 3:407–15

850

Hirano T, Minematsu K, Hasegawa Y, Tanaka Y, Hayashida K, Yamaguchi T (1994) Acetazolamide reactivity on 123I-IMP single photon emission computed tomography in patients with major cerebral artery occlusive disease: correlation with positron emission tomography parameters. *J Cereb Blood Flow Metab* 14:763–70

Huang SC, Mahoney DK, Phelps ME (1987) Quantitation in positron emission tomography: 8. Effects of nonlinear parameter estimation on functional images. *J Comput Assist Tomogr* 11:314–25

Hughes CP, Berg L, Danziger WL, Coben LA, Martin RL (1982) A new clinical scale for the staging of dementia. *Br J Psychiatry* 140:566–72

Isaka Y, Okamoto M, Ashida K, Imaizumi M (1994) Decreased cerebrovascular dilatory capacity in subjects with asymptomatic periventricular hyperintensities. *Stroke* 25:375–81

Kanno I, Iida H, Miura S, Murakami M, Takahashi K, Sasaki H, Inugami A, Shishido F, Uemura K (1987) A system for cerebral blood flow measurement using an H215O autoradiographic method and positron emission tomography. *J Cereb Blood Flow Metab* 7:143–53

Koton S, Schwammenthal Y, Merzeliak O, Philips T, Tsabari R, Orion D, Dichtiar R, Tanne D (2009) Cerebral leukoaraiosis in patients with stroke or TIA: clinical correlates and 1-year outcome. *Eur J Neurol* 16:218–25

Kozera GM, Dubaniewicz M, Zdrojewski T, Madej-Dmochowska A, Mielczarek M, Wojczal J, Chwojnicki K, Swierblewska E, Schminke U, Wyrzykowski B, Nyka WM (2010) Cerebral vasomotor reactivity and extent of white matter lesions in middle-aged men with arterial hypertension: a pilot study. *Am J Hypertens* 23:1198–203

Kudomi N, Choi E, Yamamoto S, Watabe H, Kim K, Shidahara M, Ogawa M, Teramoto N, Sakamoto E, Iida H (2003) Development of a GSO detector assembly for a continuous blood sampling system. *IEEE Trans Nucl Sci* 50:70–3

Kudomi N, Hayashi T, Teramoto N, Watabe H, Kawachi N, Ohta Y, Kim KM, Iida H (2005) Rapid quantitative measurement of CMRO(2) and CBF by dual administration of (15)O-labeled oxygen and water during a single PET scan-a validation study and error analysis in anesthetized monkeys. *J Cereb Blood Flow Metab* 25:1209–24

Kudomi N, Watabe H, Hayashi T, Iida H (2007) Separation of input function for rapid measurement of quantitative CMRO2 and CBF in a single PET scan with a dual tracer administration method. *Phys Med Biol* 52:1893–908

Meguro K, Hatazawa J, Yamaguchi T, Itoh M, Matsuzawa T, Ono S, Miyazawa H, Hishinuma T, Yanai K, Sekita Y (1990) Cerebral circulation and oxygen metabolism associated with subclinical periventricular hyperintensity as shown by magnetic resonance imaging. *Ann Neurol* 28:378–83

Mochizuki Y, Oishi M, Takasu T (1997) Cerebral blood flow in single and multiple lacunar infarctions. *Stroke* 28:1458–60

Murray AD, Staff RT, Shenkin SD, Deary IJ, Starr JM, Whalley LJ (2005) Brain white matter hyperintensities: relative importance of vascular risk factors in non-demented elderly people. *Radiology* 237:251–7

Pantoni L, Garcia JH (1997) Pathogenesis of leukoaraiosis: a review. *Stroke* 28:652–9

Powers WJ (1991) Cerebral hemodynamics in ischemic cerebrovascular disease. *Ann Neurol* 29:231–40

Pozzilli C, Itoh M, Matsuzawa T, Fukuda H, Abe Y, Sato T, Takeda S, Ido T (1987) Positron emission tomography in minor ischemic stroke using oxygen-15 steady-state technique. *J Cereb Blood Flow Metab* 7:137–42

Prins ND, van Dijk EJ, den Heijer T, Vermeer SE, Jolles J, Koudstaal PJ, Hofman A, Breteler MM (2005) Cerebral small-vessel disease and decline in information processing speed, executive function and memory. *Brain* 128:2034–41

Quarantelli M, Berkouk K, Prinster A, Landeau B, Svarer C, Balkay L, Alfano B, Brunetti A, Baron JC, Salvatore M (2004) Integrated software for the analysis of brain PET/SPECT studies with partial-volume-effect correction. *J Nucl Med* 45:192–201

Roman GC, Tatemichi TK, Erkinjuntti T, Cummings JL, Masdeu JC, Garcia JH, Amaducci L, Orgogozo JM, Brun A, Hofman A, Moody DM, O'Brien MD, Yamaguchi T, Grafman J, Drayer BP, Bennett DA, Fisher M, Ogata J, Kokmen E, Bermejo F, Wolf PA, Gorelick PB, Bick KL, Pajeau AK, Bell MA, DeCarli C, Culebras A, Korczyn AD, Bogousslavsky J, Hartmann A, Scheinberg P (1993) Vascular dementia: diagnostic criteria for research studies. Report of the NINDS-AIREN International Workshop. *Neurology* 43:250–60

Sette G, Baron JC, Mazoyer B, Levasseur M, Pappata S, Crouzel C (1989) Local brain haemodynamics and oxygen metabolism in cerebrovascular disease. Positron emission tomography. *Brain* 112(Pt 4):931–51

Streifler JY, Eliasziw M, Benavente OR, Alamowitch S, Fox AJ, Hachinski VC, Barnett HJ (2002) Prognostic importance of leukoaraiosis in patients with symptomatic internal carotid artery stenosis. *Stroke* 33:1651–5

Svarer C, Madsen K, Hasselbalch SG, Pinborg LH, Haugbol S, Frokjaer VG, Holm S, Paulson OB, Knudsen GM (2005) MR-based automatic delineation of volumes of interest in human brain PET images using probability maps. *Neuroimage* 24:969–79

Turc JD, Chollet F, Berry I, Sabatini U, Démonet JF, Ceisis P, Marc-Vergnes JP, Rascol A (1994) Cerebral blood flow, cerebral blood reactivity to acetazolamide, and cerebral blood volume in patients with leukoaraiosis. *Cerebrovas Dis* 4:287–93

Watson CC (2000) New, faster, image-based scatter correction for 3D PET. *IEEE Trans Nucl Sci* 47:1587–94

Yamanouchi H, Sugiura S, Shimada H (1990) Loss of nerve fibres in the corpus callosum of progressive subcortical vascular encephalopathy. *J Neurol* 237:39–41

Yamanouchi H, Sugiura S, Tomonaga M (1989) Decrease in nerve fibres in cerebral white matter in progressive subcortical vascular encephalopathy of Binswanger type. An electron microscopic study. *J Neurol* 236:382–7

Yamauchi H, Fukuyama H, Nagahama Y, Shiozaki T, Nishizawa S, Konishi J, Shio H, Kimura J (1999) Brain arteriolosclerosis and hemodynamic disturbance may induce leukoaraiosis. *Neurology* 53:1833–8

Yao H, Sadoshima S, Ibayashi S, Kuwabara Y, Ichiya Y, Fujishima M (1992) Leukoaraiosis and dementia in hypertensive patients. *Stroke* 23:1673–7

Yao H, Sadoshima S, Kuwabara Y, Ichiya Y, Fujishima M (1990) Cerebral blood flow and oxygen metabolism in patients with vascular dementia of the Binswanger type. *Stroke* 21:1694–9

Yokota C, Minematsu K, Ito A, Toyoda K, Nagasawa H, Yamaguchi T (2009) Albuminuria, but not metabolic syndrome, is a significant predictor of stroke recurrence in ischemic stroke. *J Neurol Sci* 277:50–3

Yonai Y, Boms N, Molnar S, Rosengarten B, Bornstein NM, Csiba L, Olah L (2010) Acetazolamide-induced vasodilation does not inhibit the visually evoked flow response. *J Cereb Blood Flow Metab* 30:516–21

*66*

# Monte Carlo simulation of scintillation photons for the design of a high-resolution SPECT detector dedicated to human brain

Yoshiyuki Hirano · Tsutomu Zeniya ·
Hidehiro Iida

## Abstract

*Objective* In a typical single photon emission computed tomography (SPECT) system, intrinsic spatial resolution depends on the accuracy of the identification of an interacting point, which is dominated by propagation of the scintillation photons in the detector block. This study was intended to establish a Monte Carlo simulation-based evaluation tool taking into account the propagation of scintillation photons to estimate the intrinsic spatial and energy resolutions of the position-sensitive scintillator block in a SPECT detector.

*Methods* We employed Geant4 Monte Carlo simulation library which incorporated the optical photon processes for two different designs of the position-sensitive scintillator blocks. The validation of the simulation code was performed for a monolithic NaI(Tl) scintillator ($251 \times 147 \times 6.4$ mm$^3$) coupled to 15 flat-panel type multi-anode photo multiplier tubes (PMT) (H8500: Hamamatsu) and results were compared with those obtained experimentally. The code was then applied to a LaBr$_3$(Ce) scintillator of 120 mm square with varied thicknesses for designing high-resolution detector.

*Results* The simulation resulted in 2.6 mm full width at half maximum (FWHM) of spatial resolution and 9.0% FWHM of energy resolution for the NaI(Tl)-based detector, which were in a good agreement of the experimental results, i.e., 2.7 mm and 10%, respectively. These findings suggest that Geant4 simulation including optical photon processes enables to predict the spatial and energy resolutions of a

SPECT detector block accurately. The simulation also demonstrated that 2 mm spatial resolution can be obtained for a 6 mm thickness of the LaBr$_3$(Ce), which is a significant improvement in performance as compared to existing gamma camera system that employs the scintillation detector fitted with PMTs.

*Conclusions* The Monte Carlo simulation-based evaluation tool was established to estimate the intrinsic spatial and energy resolutions of SPECT detector with position sensitive PMTs. This simulation may be useful to provide an optimal design of a SPECT detector without physical experiments.

**Keywords** LaBr$_3$(Ce) · Monte Carlo simulation · Geant4 · SPECT · Scintillation photon

## Introduction

Single photon emission computed tomography (SPECT) is capable of providing tomographic images of radiolabeled tracers in vivo. The equipment essentially consists of position-sensitive detectors fitted with several types of collimators, which rotate around the object to be imaged. In most SPECT detectors, the point of interaction between a gamma ray and a scintillation crystal is identified by Anger logic on a 2-dimensional domain. Interacting coordinates are calculated by a weighted mean of the deposition of scintillation photons. Spatial resolution depends on the accuracy of identification, which may be degraded as a result of the propagation of scintillation photons within the detector system.

A Monte Carlo simulation is a helpful tool in designing a new detector block. The simulation code is often useful when optimizing design parameters of the detector block,

Y. Hirano (✉) · T. Zeniya · H. Iida
Department of Bio-medical Imaging,
National Cerebral and Cardiovascular Center Research Institute,
5-7-1 Fujishiro-dai, Suita, Osaka 565-8565, Japan
e-mail: hirano@ri.ncvc.go.jp

e.g., the thickness and other geometric parameters of the scintillator as well as the scintillator material, without the need for physical experiments. In order to estimate intrinsic spatial resolution and energy resolution, it is essential to understand the process of transport of scintillation photons in the detector system, as well as the interaction of gamma rays with materials. Geant4 [1] makes it possible to simulate both these processes. Simulation studies on propagation of scintillation photons have been performed using Geant4 (or other code) [2–6]. However, it is difficult to reproduce the intrinsic spatial and energy resolutions accurately due to the many unknown factors (e.g., optical properties of materials and electrical noise) to simulate transporting scintillation photons. Resolutions essentially depend on the number of obtained scintillation photons. Geant4 does not include the optical properties of materials, such as absorption length, refraction index, and reflection. These data must be entered into Gean4 by users. The simulation accuracy is sensitive to these optical parameters. To our knowledge, a validation study on spatial and energy resolutions using Geant4 was performed only by Van Der Laan et al. [2] for a positron emission tomography (PET) instrument that employed a monolithic scintillators (LYSO(Ce): $20 \times 10 \times 10$ mm$^3$ and $20 \times 10 \times 20$ mm$^3$) and avalanche photodiodes (APD).

In this work, we intended to use Geant4 for two types of position-sensitive scintillation detector in a SPECT system. Both detectors consist of a monolithic scintillator and flat-panel type multi-anode PMTs (H8500: Hamamatsu). These are different from detectors used in previous study [2] regarding scintillator material, detector size and photosensors. With regard to photo-sensor, detection principle of PMT is absolutely different from that of APD. One detector has a larger field-of-view (FOV) and is fitted with a parallel beam collimator for imaging the whole human brain. The detector block consists of a NaI(Tl) scintillator

$(251 \times 147 \times 6.4$ mm$^3)$ and 15 PMTs. Its experimental physical performance was used to validate the simulation code, including the photon propagation processes. We then extended this simulation geometry to another detector block, which consists of a LaBr$_3$(Ce) scintillator [7, 8] coupled to 4 PMTs to achieve higher intrinsic spatial resolution. This detector has smaller FOV and may be fitted with a pinhole collimator for focused imaging of a limited area of the brain with higher spatial resolution of approximately 1 mm [9]. We also investigated effects of inclined incident angle of gamma rays into the detector in a pinhole configuration on spatial resolution of the detector system.

## Materials and methods

### Monte Carlo simulation

We employed the Monte Carlo simulation library Geant4 (version 9.2.p02) in this study. Geant4 enables us to simulate not only interaction of gamma rays with several materials but also transport of scintillation photons. In this simulation, we took into account the following electromagnetic processes: Compton scatter, photo-electric effect, Rayleigh scatter, multiple scatter, bremsstrahlung, and ionization. The first three processes involve gamma rays; the rest involve electrons. Optical photon processes in the propagation of scintillation photons were also included: absorption, Rayleigh scatter, reflection, and refraction.

Simulations were carried out for essentially two sets of detector configurations as follows. The two sets of detector configurations (large-FOV detector and small-FOV detector) were precisely reproduced as shown in Fig. 1. The simulation configurations included scintillator, reflector, optical window, optical grease, PMT window, and PMT cathodes. Gamma rays entered the detector vertically,
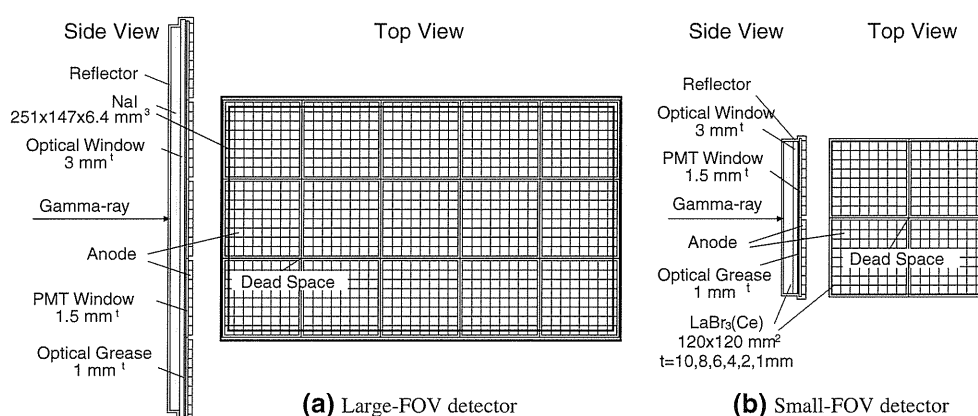


**Fig. 1** Geometrical configurations of the large-FOV detector (**a**) and the small-FOV detector (**b**). In the simulation, we included the scintillator, reflector, optical window, optical grease, PMT window, and PMT anodes. The scintillator thickness of the small-FOV detector was varied (10, 8, 6, 4, 2, and 1 mm)

except for the simulation carried out for a pinhole configuration. When a gamma ray interacted with the scintillator and deposited its energy, scintillation photons were emitted isotropically. The emission spectra of NaI(Tl) and LaBr$_3$(Ce) are shown in Fig. 2a. The number of scintillation photons followed the Poisson distribution, and the mean was proportional to the energy deposition (LaBr$_3$(Ce): 63 photons/keV; NaI(Tl): 38 photons/keV). The scintillation photons propagated in the scintillator, optical window, optical grease and PMT window. At the reflector, the Lambert reflection was applied. The reflectance was 0.95 (white plastic). For a photon that was not reflected, propagation was terminated. At other boundaries between materials, the Fresnel reflection or Fresnel refraction was applied. When scintillation photon reached a cathode, the detection was determined by the quantum efficiency (Fig. 2a, gray line) and the collection efficiency (60%) of the H8500. The interacting point was reconstructed by Anger logic. An error of 17% was assigned to the anode gain. The error was estimated from anode uniformity map described in the specification. Transmittances of NaI(Tl) and borosilicate glass are shown in Fig. 2b. PMT cathodes and dead space surrounding the cathodes were assumed to be perfect absorbers. This simulation did not include absorptions by LaBr$_3$(Ce) and optical grease, because these transmittance data are not available. However, according to [10], the absorption for visible light is low. The thickness of optical grease was assumed as 1 mm. Refractive indices of, NaI(Tl), LaBr$_3$(Ce) and optical grease are 1.85, 1.9 and 1.465, respectively. With regard to borosilicate glass, the index was shown in Fig. 2c. These data were obtained from each specification.

## Validation of the simulation code

To validate the Monte Carlo simulation, we compared spatial and energy resolutions obtained from the simulation with experimental values for the large-FOV detector. The experimental setup was as follows. The detector consisted of a monolithic NaI(Tl) scintillator (Saint-gobain) of $251 \times 147 \times 6.4$ mm$^3$, fitted to 15 flat-panel type multianode PMTs (H8500: Hamamatsu) arranged in a $5 \times 3$ array. Each of the PMTs had 64 cathodes ($8 \times 8$ array) that measured 5.8 mm square (6.08 mm pitch at center). The size of each PMT was $52 \times 52$ mm$^2$, and the PMT window was a 1.5 mm thickness of borosilicate glass that was transparent to visible lights. The NaI(Tl) scintillator was covered with a white diffuse reflector and an optical window of 3 mm thickness at the connection side of the PMTs. The optical window was also made of borosilicate glass. The NaI(Tl) scintillator was coupled to the PMTs by optical grease (BC630: Saint-gobain). Electric resistance arrays were connected to the anode outputs. The sum of the anode outputs and the positional coordinate ($x$, $y$) calculated by Anger logic were recorded in list mode. A specially designed collimator was placed in front of the detector block. The collimator was a $300 \times 200 \times 10$ mm$^3$ block of lead with 170 holes of 1.5 mm diameter arranged in a $17 \times 10$ grid pattern with a grid interval of 15 mm. Small-tube sources (7 mm diameter) filled with Tc-99m solution were placed on 170 collimator holes, and position dependency of the energy spectra and point spread functions were measured. Energy and spatial resolutions were then evaluated.

In the simulation, spatial and energy resolutions were evaluated for the NaI(Tl)-based large-FOV detector by exposing 3000 gamma rays (141 keV) to the detector as a parallel beam with a circular distribution of 1.5 mm diameter at each of the hole positions. Interactions with the collimator were not included to reduce the computing time.

## Application to the design of a new detector

Another series of simulations were carried out for the small-FOV detector to optimize the geometrical parameters. The scintillator was assumed to be LaBr$_3$(Ce) with a surface area of $120 \times 120$ mm$^2$. The scintillator was coupled to 4 PMTs (H8500) arranged in a $2 \times 2$ array. The
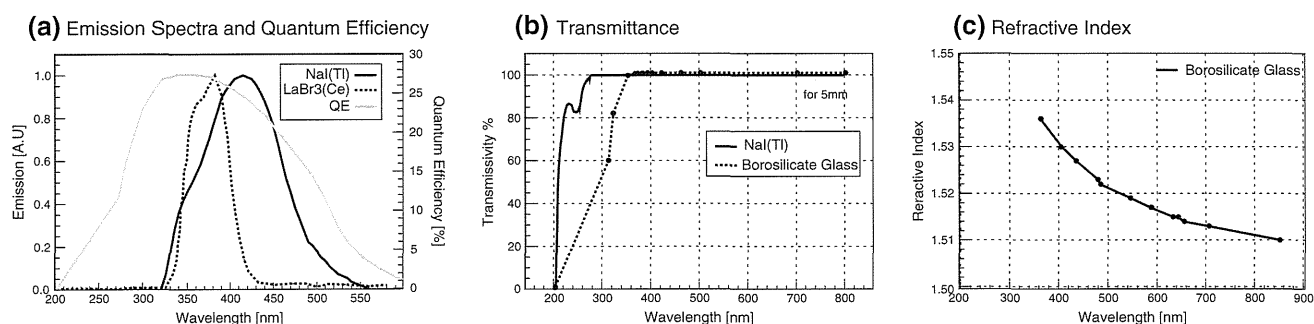


Fig. 2 a Emission spectra of NaI(Tl) (*solid line*) and LaBr$_3$(Ce) (*dotted line*) (BrilLanCe350: Saint-gobain) together with the quantum efficiency of the H8500 (*gray line*). b Transmittance of NaI(Tl) and borosilicate glass (assumed BK7: Schott Glass). c Refractive index of borosilicate glass. These data are available from each specification

surface of the scintillator was covered with a white diffuse reflector. The thickness of the scintillator was varied (10, 8, 6, 4, 2, and 1 mm) and the optical window thickness was also varied (1 and 3 mm). Simulation was also carried out using NaI(Tl) instead of $LaBr_3(Ce)$ as the reference. Additional simulations were performed to evaluate effects of varying incident angle for a detector fitted with a pinhole collimator. Finally, detection efficiency defined as follows was estimated

$$\text{Efficency} = \frac{\text{Number of full energy despitions}}{\text{Number of incident gamma rays}}.$$

Densities of NaI(Tl) and $LaBr_3(Ce)$ were 3.67 and 5.08 $g/cm^3$, respectively.

Gamma rays (141 keV) entered the scintillator vertically at 49 positions on a $7 \times 7$ grid with 15 mm intervals, similar to the source position of the large-FOV detector. In the pinhole configuration, gamma rays were generated at a point 86.6 mm above the center of the detector to the 49 positions. The maximum incident angle was 60°. 1000 gamma rays were simulated at each position.

Analysis

In both the simulation and experiment, the spatial and energy resolutions were evaluated at every grid points as follows. Photo-peak of 141 keV was fitted using a Gauss function, and 3-sigma region as an energy window (e.g., 116–164 keV for the experiment with NaI(Tl)) was selected. Using energy-selected events, interacting points were reconstructed by Anger logic and projected into the $x$ and $y$ directions. The spatial resolution was calculated by fitting with a function that took into account the diameter of holes, expressed as follows:

$$f(x) = \int g(x) \times h(z - x)dx$$
$$= \frac{1}{2a}\left\{\text{erf}\left(\frac{a + b - x}{\sqrt{2}\sigma}\right) - \text{erf}\left(\frac{b - x}{\sqrt{2}\sigma}\right)\right\},$$

$f(x)$ is assumed to be a convolution function of the Gauss function $g(x)$, which serves as a point spread function, and the uniform distribution $h(x)$, which describes the source distribution. erf is an error function, $a$ is the diameter of a hole, and $b$ is the position of a hole. The spatial resolutions for each position were calculated according to the term $\sqrt{8\ln 2} \times \sigma$, where $\sigma$ is the standard deviation of the Gauss function. Finally, the energy resolution was derived from the energy spectra at each position. In this analysis of the experiment, background counts were subtracted from the experimental data.

We compared spatial resolution (FWHM mm) and energy resolution (FWHM %) with experimental results of the large-FOV detector. The planar image, spatial resolution in $x$ and $y$ direction, energy spectra, and their average resolutions were used for the comparisons. Finally, the small-FOV detector was designed to optimize spatial resolution and detection efficiency.

Results

Validation of simulation code

Planar images of multiple point sources obtained from the experiment and the simulation for the large-FOV detector are shown in Fig. 3. It can be seen that intervals between points are constant around the center, but becomes closer at the edge. The spatial resolution in the $x$ direction along the central line is shown in Fig. 4. The spatial resolutions are almost homogenous around the center but become gradually worse at the edge of the detector in both the simulation and experiment. In the simulation, spatial resolution agreed with the experimental results within approximately 10% at $\pm$ 105 mm distance from the center. At the position 10 mm away from the detector edge, the resolutions become relatively worse. The experimental mean resolution, omitting those from the edge, were 3.6 and 3.1 mm in
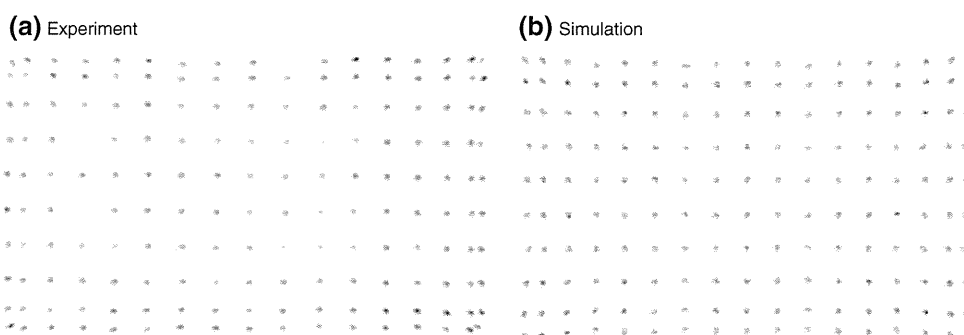
**(a)** Experiment　　　　　　　　　　　　　　　　**(b)** Simulation

**Fig. 3** Planar images of multiple point sources obtained from experiment (**a**) and simulation (**b**). These interacting points are calculated by Anger logic
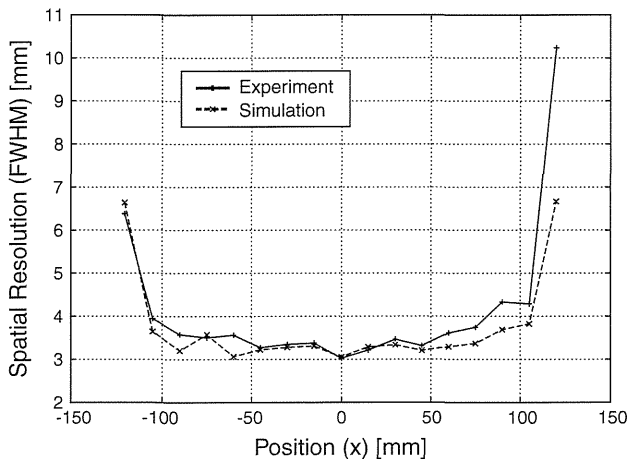
**Fig. 4** Comparison of spatial resolutions in the *x* direction. The resolutions are for lines from the 5th row from the bottom in Fig. 3. The *solid line* shows the experimental result, and the *dotted line* shows the simulation result
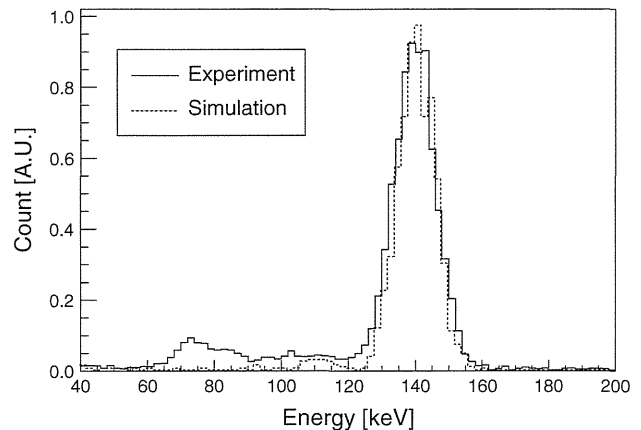


**Fig. 5** Energy spectra at the center of the detector. The *solid line* shows experimental results; the *dotted line* shows the simulation. In the simulation, energy spectra are derived from the number of obtained scintillation photons

the *x* and *y* directions, respectively. The best resolutions in the *x* and *y* directions were 3.0 and 2.7 mm; these were obtained at the center. In the simulation, the mean resolutions in the *x* and *y* directions were 3.3 and 3.0 mm, respectively. The best resolutions were 2.8 and 2.6 mm for the *x* and *y* directions. Figure 5 shows the energy spectra at the center. The broadness of the peak in the simulation corresponds to the fluctuation of the number of obtained scintillation photons. The energy resolutions determined from spectra of the experiment and the simulation were 10.0 and 9.0% (FWHM), respectively. With respect to energy resolution, clear position dependence was not observed. The mean and deviation of energy resolution of the experiment and the simulation, respectively, were 10.3 ± 0.2 and 9.3 ± 0.3%.

## Application of the simulation code for designing high-resolution detector

The simulation results of planar images of multiple point sources for the small-FOV detector with different thicknesses (10, 6 and 1 mm) are shown in Fig. 6. Clear separation of source positions was obtained in the thin scintillator, especially the 1 mm thickness. As the scintillator was thicker, interval of source positions decreased and the point spread function blurred. The mean spatial resolutions with thicknesses of 10, 8, 6, 4, 2, and 1 mm are shown in Fig. 7a together with the cases in which the scintillator is NaI(Tl), the thickness of the optical window is 1 or 3 mm, and the angle of incidence is oblique. In these configurations, comparable resolutions in the *x* and *y* directions were obtained. $LaBr_3(Ce)$ had better spatial resolution than NaI(Tl) by 22–36%. The best resolution was 0.76 mm with 1 mm thickness. Energy spectra obtained

from $LaBr_3(Ce)$ and NaI(Tl) of 1 mm thickness at the center of the detector were shown in Fig. 8. The numbers of obtained scintillation photons in an event of full energy deposition (141 keV) were 5039 and 3103, resulting in energy resolution of 8.65 and 11.7%, respectively. The detection efficiencies are shown in Fig. 7b. The maximum efficiency for the 141 keV gamma rays was 93% with 10 mm thickness. The efficiency decreased with thinner scintillator (26% for 1 mm thickness). Varying the optical window between 1 and 3 mm had little effect. For the oblique incident cases, the spatial resolution became slightly worse by several percent.

Figure 9 shows an average distribution of scintillation photons on the 16 × 16 anodes in the case of 1000 gamma rays entering the of the detector. The thicker scintillator has a wider spread of scintillation photons.

## Discussion

### Adequacy of the simulation

This study demonstrates the adequacy of the simulation code. Both the spatial resolution and the energy resolution appeared to be well reproduced between simulation and experimental data. It has thus been suggested that Geant4 with optical photon processes would be of use when one intends to optimize the design of a new scintillation detector assembly. However, the simulation systematically exhibited small but significant overestimations compared with the experimental data. This can probably be attributed to additional errors in the experiments, which have not been taken into account in the simulation. Potentially influential factors include electrical noise and/or uncertainties in the multiplying processes of the PMTs. The angular
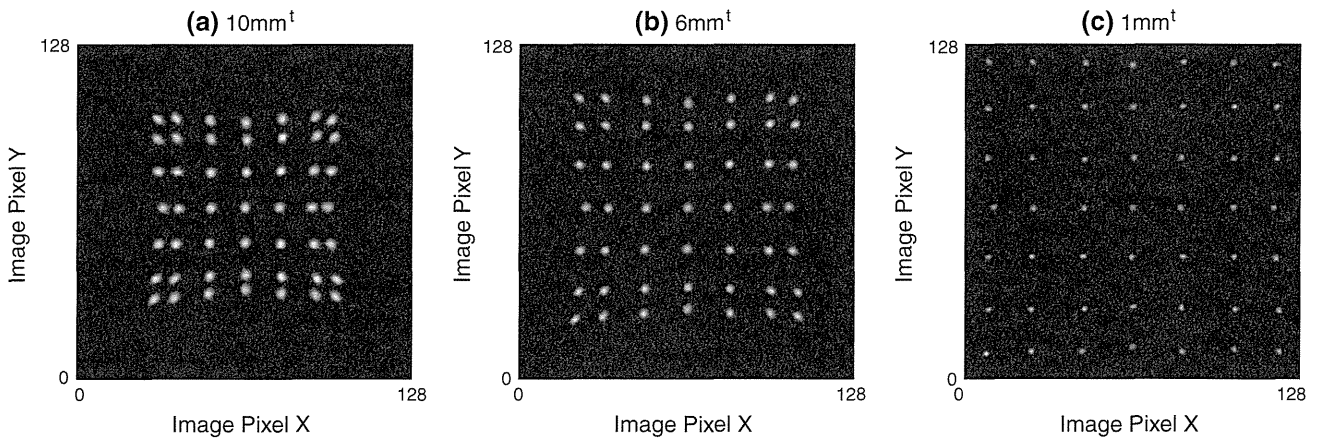
**(a)** 10mm$^t$      **(b)** 6mm$^t$      **(c)** 1mm$^t$

**Fig. 6** Reconstruction of interacting points with a simulated LaBr$_3$(Ce) scintillator with thickness 10 mm (**a**), 6 mm (**b**), or 1 mm (**c**). 141 keV gamma rays entered the LaBr$_3$(Ce) scintillator vertically at 49 positions arranged in a 7 × 7 grid pattern with 15 mm intervals. Thinner scintillators have better spatial resolutions. Good separations and position linearity were obtained with a 1-mm thickness
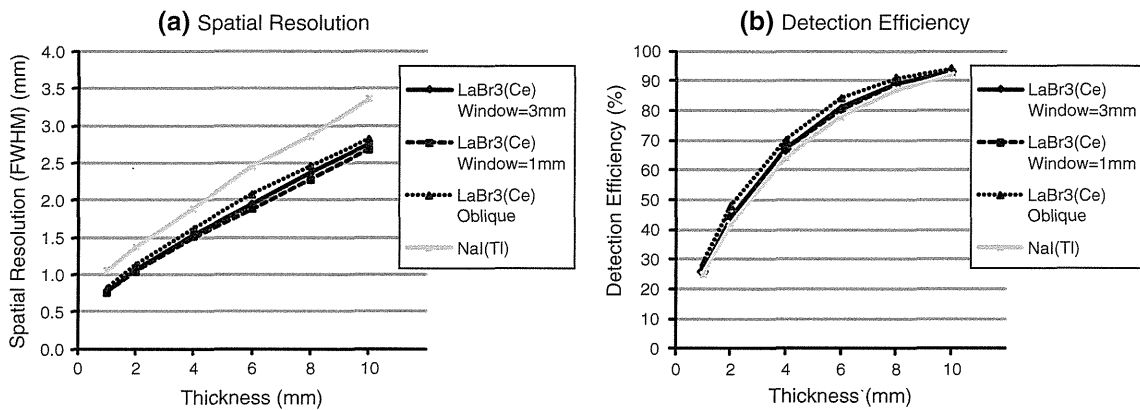


**(a)** Spatial Resolution      **(b)** Detection Efficiency

**Fig. 7** Spatial resolutions (FWHM, mm) and detection efficiency (%) of the small-FOV detector estimated by simulation. Thickness was varied from 10 to 1 mm."OpWin" stands for the optical window. "Oblique" means that gamma rays enter the scintillator at an oblique angle
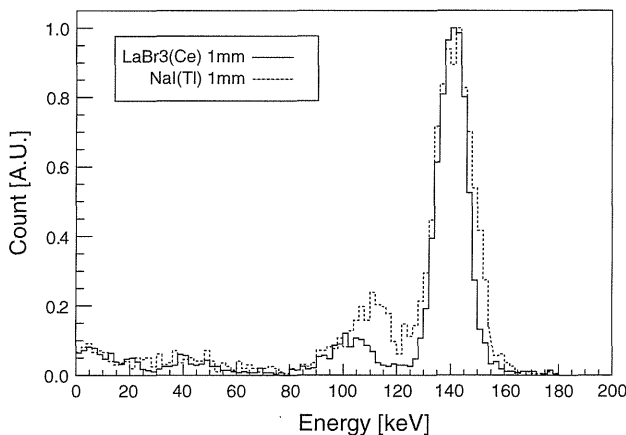


**Fig. 8** Energy spectra LaBr$_3$(Ce) (*solid line*) and NaI(Tl) (*dot line*) of 1 mm thickness at the center of the small FOV detector normalized by the maximum counts. Energy resolutions of LaBr$_3$(Ce) and NaI(Tl) were 8.65 and 11.7%, respectively

distribution of the source is also considered as an influential factor. The beam was parallel in the simulation, but there were slight obliquely incidents in the experiment. Differences in the spatial resolution in the $x$ and $y$ directions can be attributed to difference of the number of cathodes along the $x$ and $y$ axes. The larger number of cathodes causes a larger uncertainty in the position identification due to the statistical fluctuation of scintillation photons at each anode. Note that the simulation of a square detector geometry for the small-FOV detector resulted in comparable resolutions for both the $x$ and $y$ directions. The spatial resolution has a position dependency, and decreases near the edge. This is because the distribution of the scintillation photons entering the cathodes is isotropic at the center, while scintillation photons partially reflect at the edge, resulting in an asymmetrical distribution at the edge of the detector. This caused decreased linearity performance and degraded spatial
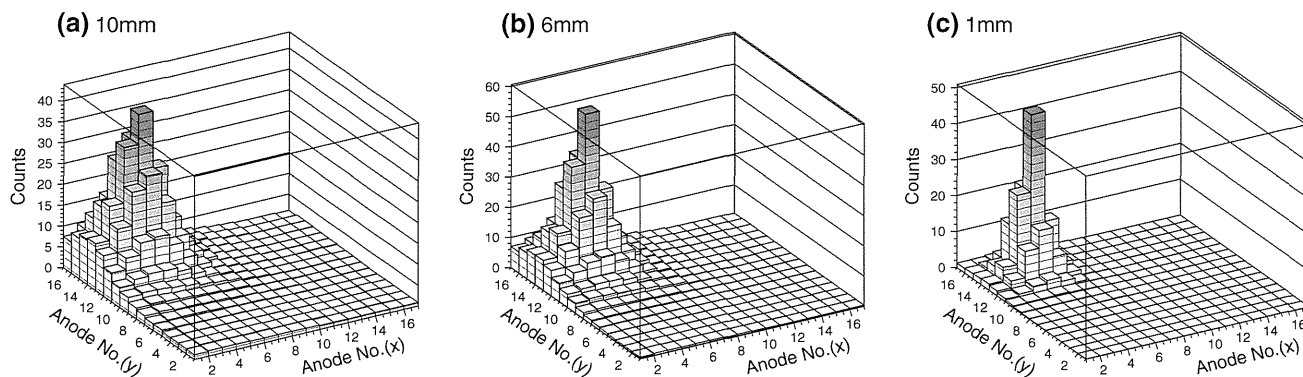
**Fig. 9** Average distribution of scintillation photons on the 16 × 16 array of anodes. Gamma rays enter the edge of the detector. Scintillator thickness is 10 mm (**a**), 6 mm (**b**), or 1 mm (**c**)

resolution near the edge. Energy resolution depends on the number of observed scintillation photons. Homogeneous energy resolution indicates that the correction efficiencies of scintillation photons are almost equal over the entire detector. Importantly, the energy resolution was highly reproducible without any arbitrary parameters. It is often the case in most Monte Carlo simulation studies that energy resolution is fitted to match the experimental results. However, this simulation can reproduce the energy resolutions for a given set of detector design parameters. This is one of the most important features of this study. The simulated energy spectrum of the scatter region (below 120 keV) was different from the experimental results. It was probably due to the scatter from the collimator in the experiment. The simulation did not include interaction with the collimator.

Conceptual design of high-resolution SPECT system for human brain

We performed the simulation for optimizing a new high-resolution detector system for SPECT described in [9]. A pinhole collimator can be adopted to achieve the high spatial resolution typically achieved with a small-FOV. The reconstructed FOV can, however, be truncated if applied to an object which is larger than the FOV; this truncation can cause artifacts in the reconstructed images, and errors in the quantitative pixel counts. A new technique for truncation-compensated 3D-OSEM reconstruction [11], based on the theory proposed by Kudo et al. [12], could be one application of the two detectors presented in this study. One detector, with an NaI(Tl)-based large-FOV detector, provides an image without truncation, and is used as a supporting information for reconstructing truncated data from the small-FOV detector successfully. The small-FOV detector has the potential to provide high resolution of approximately 1 mm, but with possible truncation. Thus, the combination of the two types of detectors may provide

SPECT images with both high spatial resolution and the quantitative accuracy of a magnified FOV. To achieve such a high resolution in practice, a prior high-accuracy estimate is essential. Monte Carlo simulation code, validated for a scintillator based on multi-anode PMTs, would be helpful for optimizing and validating various design configurations.

Design of the small-FOV detector with high resolution

LaBr$_3$(Ce) is a promising material for use in scintillator crystals to achieve higher resolution than NaI(Tl); this is primarily due to the larger amount of scintillation photons, as demonstrated in this study. The thinner scintillator provides better spatial resolution, because thinner scintillators prevent the spread of scintillation photons, as shown in Figs. 6, 7 and 9. However, efficiency decreases with a thinner scintillator crystal, resulting in reduced sensitivity of gamma-ray detection. Thus, there is a trade-off between spatial resolution and detection efficiency. A thickness of 6 mm appeared to be best suited for our detector system, as we originally aimed at achieving a spatial resolution ∼ 1 mm with sufficient detection efficiency. If we use a pinhole collimator with 0.5 mm diameter and threefold magnification factor, an intrinsic spatial resolution of ∼ 2 mm would provide the spatial resolution of 1 mm in a SPECT system [13]. The simulation demonstrated that a 6 mm thickness of LaBr$_3$(Ce) can provide ∼ 2 mm intrinsic spatial resolution and a detection efficiency of approximately 86% for Tc-99m, that efficiency is comparable to the performance of currently popular SPECT detectors. Using a pinhole collimator, spatial resolution could be slightly worse; this would be attributed to the spread of interaction points in the x–y plane due to the oblique angle of incidence. To evaluate the differences between vertical and oblique angles of incidence, it is necessary to simulate both gamma rays and scintillation photons, as we have done in this simulation study. Geant4 is of use for such evaluations, because it takes both processes into account.

Detector systems that consist of a monolithic scintillator and multi-anode PMTs have the potential to improve spatial resolution over what is currently achievable. In this study, Anger logic using all anodes was employed to identify an interacting point. Anger logic using a subset of anodes will improve the spatial resolution, the nearest-neighbor algorithm [14], and nonlinear least squares method [15] are also promising methods. In the future, in order to employ these methods, analog-to-digital converters (ADC) for all anodes will be installed in our detector systems.

## Conclusion

We performed the Geant4 simulation that took into account propagation of gamma rays and transport of scintillation photons. The simulation reproduced experimental results with regard to both spatial resolution and energy resolution for a SPECT detector based on NaI(Tl) scintillator and position sensitive PMTs (H8500). We demonstrated a simulation for a design of the small-FOV detector to optimize geometrical parameter. This simulation may be useful to provide an optimal design of a SPECT detector without physical experiments.

## References

1. Agostinelli S, Allison J, Amako K, Apostolakis J, Araujo H, Arce P, et al. GEANT4 a simulation toolkit. Nucl Instrum Methods Phys Res A. 2003;506:250–303.
2. Van Der Laan DJ, Dennis RS, Maas MC, Beekman FJ, Bruyndonckx P, van Eijk CWE. Optical simulation of monolithic scintillator detectors using GATE/GEANT4. Phys Med Biol. 2010;55:1659–75.
3. Sergio LM, Giuseppe B, Paolo B, Dante B, Valentino OC, et al. Optical physics of scintillation imagers by GEANT4 simulations. Nucl Instrum Methods Phys Res A. 2009;607:259–60.
4. Ciocia F, Braem A, Chesi E, Leo RD, Joram C, Lagamba L, et al. GEANT4 studies on the propagation and detection of scintillation light in long thin YAP crystals. Nucl Instrum Methods Phys Res A. 3009;600:506–12.
5. Wirth S, Metzger W, Pham-Gia K, Heismann BJ. Impact of photon transport properties on the detection efficiency of scintillator arrays. IEEE Nuclear Sci Symp Confer Record. 2006; 2602–3
6. Soreefan AM, Hui T, DeVol TA, Dept. Experimental and monte carlo investigation of the light collection efficiency of heterogenous scintillation flow cell detectors. IEEE Nuclear Sci Symp Confer Record. 2003;760–2
7. Pani R, Pellegrini R, Cinti MN, Bennatia P, Bettia M, Vittorinia F, et al. LaBr3:Ce crystal: the latest advance for scintillation cameras. Nucl Instrum Methods Phys Res A. 2007;572:268–9.
8. Pani R, Cinti MN, Pellegrinia R, Bennatia P, Bettia M, Vittorinia F, et al. LaBr3:Ce scintillation gamma camera prototype for X and gamma ray imaging. Nucl Instrum Methods Phys Res A. 2007;576:15–8.
9. Zeniya T, Hirano Y, Sakimoto T, Ishida K, Watabe H, Teramoto T, et al. Conceptual design of high resolution and a quantitative SPECT system for imaging a selected small ROI of human brain. IEEE Nuclear Sci Symp Confer Record. 2009; 3484–6
10. Li C, Wang B, Wang R, Wang H, Zhu Z. First-principles study of the electronic and optical properties of lanthanide bromide. Thin Solid Films. 2008;516:7894–8.
11. Zeniya T, Watabe H, Inomata T, Iida H, A Sohlberg, H Kudo. 3DOSEM reconstruction from truncated data in pinhole SPECT. IEEE Nuclear Sci Symp Confer Record. 2007; 4205–7
12. Kudo H, Courdurier M, Noo F, Defrise M. Tiny a prior knowledge solves the interior problem in computed tomography. Phys Med Biol. 2008;53:2207–31.
13. Jaszczak RJ, Li J, Wang H, Zalutsky MR, Coleman RE. Pinhole collimation for ultra-high-resolution small-field-of-view SPECT. Phys Med Biol. 1994;39:425–37.
14. Maas MC, Schaart DR, Van Der Laan DJ, Bruyndonckx P, Lemaitre C, Beekman FJ, et al. Monolithic scintillator PET detectors with intrinsic depth-of-interaction correction. Phys Med Biol. 2009;54:1893–908.
15. Zhi Li, Wedrowski M, Bruyndonckx P, Vandersteen G. Nonlinear least-squares modeling of 3D interaction position in a monolithic scintillator block. Phys Med Biol. 2010;55:6515–32.

# ORIGINAL ARTICLE

# Effects of patient movement on measurements of myocardial blood flow and viability in resting $^{15}$O-water PET studies

Kazuhiro Koshino, PhD,[a] Hiroshi Watabe, PhD,[b] Junichiro Enmi, PhD,[a]
Yoshiyuki Hirano, PhD,[a] Tsutomu Zeniya, PhD,[a] Shinji Hasegawa, MD,[c]
Takuya Hayashi, MD,[d] Shigeru Miyagawa, MD,[e] Yoshiki Sawa, MD,[e]
Jun Hatazawa, MD,[b] and Hidehiro Iida, DSc[a]

*Background.* Patient movement has been considered an important source of errors in cardiac PET. This study was aimed at evaluating the effects of such movement on myocardial blood flow (MBF) and perfusable tissue fraction (PTF) measurements in intravenous $^{15}$O-water PET.

*Methods.* Nineteen $^{15}$O-water scans were performed on ten healthy volunteers and three patients with severe cardiac dysfunction under resting conditions. Motions of subjects during scans were estimated by monitoring locations of markers on their chests using an optical motion-tracking device. Each sinogram of the dynamic emission frames was corrected for subject motion. Variation of regional MBF and PTF with and without the motion corrections was evaluated.

*Results.* In nine scans, motions during $^{15}$O-water scan (inter-frame (IF) motion) and misalignments relative to the transmission scan (inter-scan (IS) motion) larger than the spatial resolution of the PET scanner (4.0 mm) were both detected by the optical motion-tracking device. After correction for IF motions, MBF values changed from $0.845 \pm 0.366$ to $0.780 \pm 0.360$ mL/minute/g ($P < .05$). In four scans with only IS motion detected, PTF values changed significantly from $0.465 \pm 0.118$ to $0.504 \pm 0.087$ g/mL ($P < .05$), but no significant change was found in MBF values.

*Conclusions.* This study demonstrates that IF motion during $^{15}$O-water scan at rest can be source of error in MBF measurement. Furthermore, estimated MBF is less sensitive than PTF values to misalignment between transmission and $^{15}$O-water emission scans. (J Nucl Cardiol 2012;19:524–33.)

Key Words: Myocardial blood flow • water-perfusable tissue fraction • PET • myocardial perfusion imaging • motion correction • $^{15}$O-labeled water

## INTRODUCTION

Positron emission tomography (PET) has been extensively utilized for a wide range of non-invasive functional imaging of the myocardium in vivo. When using this method, the global body movements of patients could be a source of quantitative errors. Such

524

movement could be particularly problematic when scans are carried out for a relatively long period.[1,2] Problems also arise when studies are carried out during physiologically stressed conditions, e.g., a cycling exercise in the PET scanner.[3] Errors can be attributed not only to the mismatch between the emission and the transmission data but also to the patient motion during each of the emission and/or the transmission scans.[3]

$^{15}$O-water PET studies provide quantitative information regarding myocardial blood flow (MBF) and coronary flow reserve (CFR), as well as a marker of myocardial viability, termed the water perfusable tissue fraction (PTF) or water perfusable tissue index (PTI).[4-12] The distribution of radioactivity during $^{15}$O-water PET varies over time; this poses challenges for software-based correction of patient movement. Naum et al proposed to correct for such motion based on the rigid body model by aligning two external radioactive markers on the back of each subject. This study was conducted by performing dynamic scans while the subjects were under resting conditions and engaged in a cycling exercise.[3] Although no correction was made for the misalignment between transmission and emission scans, their study demonstrated reasonable improvement in calculated MBF values.

In our previous work, we developed an alternative system that uses an optical motion-tracking device to detect and correct for the patient's global movement during a cardiac $^{15}$O-water PET study.[13] Our system provides a correction for movement during dynamic scanning, as well as for misalignment between the transmission and the emission scans, to compensate for errors in attenuation correction procedures. We evaluated and methodologically validated the inherent accuracy of this system in a cardiac phantom study. The correction for simulated global movement in a $^{15}$O-water cardiac PET study of a healthy volunteer has also demonstrated reasonable regional MBF values, compared to values not adjusted for movement.

The purpose of this study was to evaluate the effects of global movements of subjects on quantification of MBF and PTF. Our previously validated system was used to detect and correct for the global movements of healthy volunteers, as well as patients who have suffered from severe cardiac dysfunction, during $^{15}$O-water PET studies under resting conditions.

## METHODS

### Subjects

Subjects consisted of 10 healthy volunteers and 3 patients with previous myocardial infarction. The volunteers were all male, 22-32 years of age (mean ± 1standard deviation (SD)

25 ± 3 years). The volunteers had no signs or symptoms of ischemic heart disease. Patients were studied before and after the cell transplantation therapy with autologous myoblast sheets (AMS).[14,15] Scans were carried out by independent clinical research project, but were included in this study by mutual agreement. Two of the patients were male, the other was female; patients were 43-63 years of age. All patients had left ventricular assist systems (LVASs) at the time of PET study, except for one patient who received LVAS after the first PET and before the second PET studies. The PET studies were carried out 67-104 days (mean ± SD 82 ± 19 days) after the implantation of LVASs, and 26-106 days (mean ± SD 56 ± 44 days) after AMS transplantation therapy. All subjects gave written informed consent according to a protocol approved by the Ethical Committee and Internal Review Board of Osaka University.

### PET Scan

The PET scanner was a HEADTOME-V tomograph (SHIMADZU Corp., Kyoto, Japan).[16] All data were acquired in 2D mode. Reconstructed images were obtained using a filtered back-projection algorithm with a Gaussian filter of 9 mm (full width at half maximum). The matrix and voxel sizes of reconstructed image were 128 × 128 × 63 and 2.03 × 2.03 × 3.13 mm$^3$, respectively. No scatter correction was applied to the image reconstruction.

Each subject was laid on the bed of the PET camera without any fixation of the body, and scanned at rest. A transmission scan was carried out first for correction of photon attenuation (20 minutes on the healthy volunteers, 10-15 minutes on the patients). A $^{15}$O-CO emission scan for blood pool imaging was initiated 8 minutes after inhalation of $^{15}$O-CO gas for 2 minutes (3.0-3.2 GBq). The $^{15}$O-water dynamic emission scan was then carried out following intravenous administration of $^{15}$O-water (1.1 GBq over 40 seconds) into the brachial vein, except for one patient who received the administration via right femoral vein. $^{15}$O-water scans were performed for 6 minutes, using 26 dynamic frames consisting of 12 × 5 s, 8 × 15 s, and 6 × 30 s. $^{15}$O-water scans were performed only once on eight healthy volunteers; two of the volunteers underwent $^{15}$O-water scans twice. Thus, a total of twelve $^{15}$O-water scans were carried out on the healthy volunteers. One patient underwent PET scans three times (before and after the implantation of LVAS, and after the cell transplantation therapy); the other two were scanned twice (before and after the cell transplantation therapy). Thus, a total of seven PET studies were carried out on the patients.

### Motion Detection and Correction

Subject motion during cardiac $^{15}$O-water PET was detected using an optical motion-tracking device, POLARIS (Northern Digital Inc., Canada). This method for motion correction (MC) is based on a rigid body model, and performed on each sinogram of the dynamic frame to correct for inter-scan (IS) and inter-frame (IF) motions, as shown in Figure 1. The correction process was performed automatically, based on
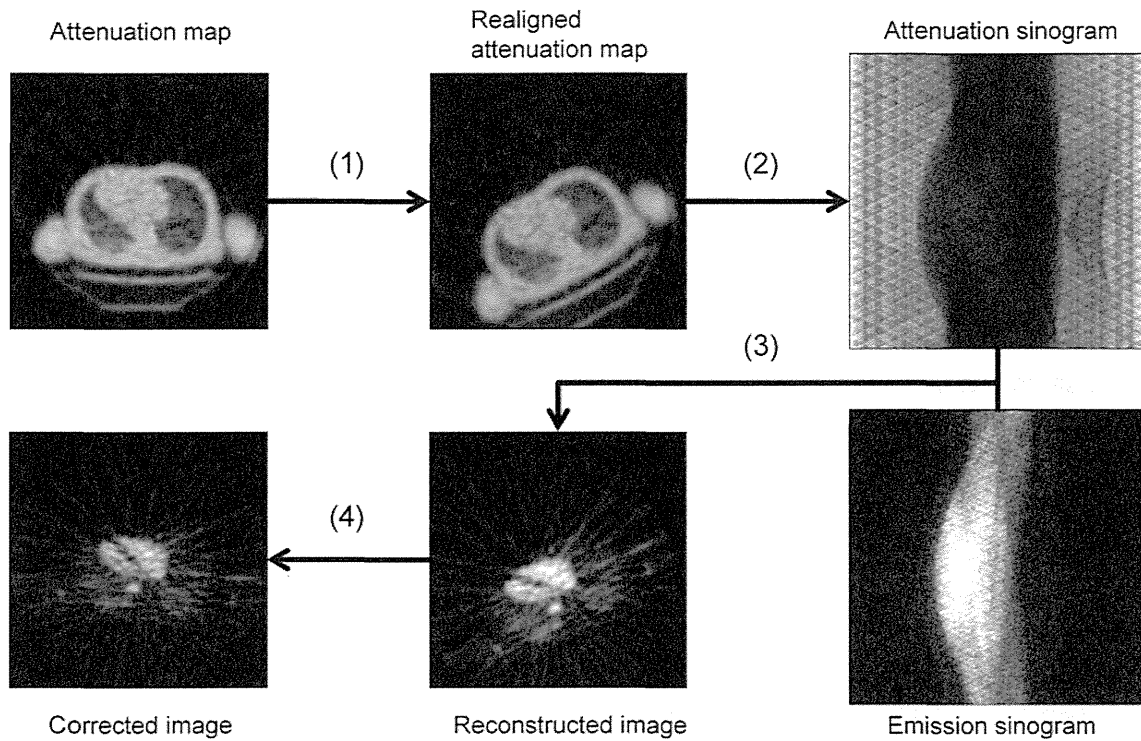
Attenuation map

Realigned
attenuation map

Attenuation sinogram

(1)

(2)

(3)

(4)

Corrected image

Reconstructed image

Emission sinogram

**Figure 1.** Schematic diagram of the correction for IS and IF motions.

user input consisting of subject locations measured by POLARIS, sinograms, and reconstruction parameters. In this manuscript, the IS motion denotes global motion between transmission and the first frame of $^{15}$O-water emission scan; the IF motion, which is in addition to the IS motion, denotes global motion between frames of the $^{15}$O-water scan. Methodological details regarding detection and correction of the motions are described in our previous studies.[13,17,18]

## Motion Classification

Global movement during $^{15}$O-water scan was characterized as consisting of IS and IF motions. Accordingly, motion was classified as: (1) IS + IF, in which both IS and IF motions were present; (2) IS motion only; (3) IF motion only; and (4) neither type of movement was present (NE). The presence of each IS and IF motion was determined as described below. Using values $t_x(i)$, $t_y(i)$, and $t_z(i)$ to represent translational movement in the $x$, $y$, and $z$, respectively, directions between the transmission and the $i$th frame of the $^{15}$O-water scans, IS motion was considered significant if $\sqrt{t_x(1)^2 + t_y(1)^2 + t_z(1)^2} > 4.0\,\text{mm}$, where the value of 4.0 mm was the intrinsic spatial resolution of the PET scanner.[16]

IF motion was considered to be significant if $\max\{L(i), H(i)\} > 4.0\,\text{mm}$, where $L(i)$ represents the gradual movement of the subject during the scan, and $H(i)$ denotes the motion between adjacent frames. These two components of the IF motion can be expressed as

$$L(i) = \sqrt{\sum_{w=x,y,z} [t_w(i) - t_w(1)]^2} \qquad (1a)$$

$$H(i) = \sqrt{\sum_{w=x,y,z} [t_w(i) - t_w(i-1)]^2} \qquad (1b)$$

## Motion Effect Evaluation

To evaluate motion effects on perfusion and viability measurements, we estimated regional MBF and PTF values for nine myocardial segments (anterior, lateral, posterior, and septal wall regions at middle and basal levels, as well as apex) with and without MCs, as described in the following section. Percent differences in the estimated values between with and without MCs for the nine myocardial regions were statistically tested using a one-way ANOVA to find myocardial segments sensitive to global movement. The percent differences were employed owing to avoiding difference of physiological states cross the subjects. The percent difference was defined by $\%\Delta q(i) = 100 \times |q_W(i) - q_{WO}(i)|/q_{WO}(i)$, where $q_W(i)$ and $q_{WO}(i)$ are MBF or PTF values, respectively, for the $i$th myocardial segment with and without MCs. Absolute values of MBF and PTF with and without MCs for each group were also assessed using Bland-Altman analysis and a paired 2-tailed $t$ test. In the IS + IF motion group, to assess the effects of IS and IF motions, additional MBF and PTF estimations were performed on the data from $^{15}$O-water images corrected for IS motions (IS + IF − IS) and also on data corrected for IF motions (IS + IF − IF). The quantitative values obtained from IS + IF − IS data were considered to be affected by IF